Estimates of Crystallinity utilizing Differential Scanning Calorimetry: Application to the Kīlauea 2018 lower East Rift Zone Eruption Corresponding Author: Halverson, B.A.¹, ¹Department of Earth and Planetary Sciences, University of Texas at San Antonio, San Antonio, TX, 78249 Emerson, A.¹, ¹Department of Earth and Planetary Sciences, University of Texas at San Antonio, San Antonio, TX, 78249 Hammer, J.², ²Department of Earth Sciences, University of Hawai'i at Mānoa, Honolulu HI Lira, J.¹, ¹Department of Earth and Planetary Sciences, University of Texas at San Antonio, San Antonio, TX, 78249 Whittington, A.¹, ¹Department of Earth and Planetary Sciences, University of Texas at San Antonio, San Antonio, TX, 78249

ABSTRACT

31

Rocks produced by diverse processes, from condensation in space to impacts on planetary 32 surfaces to volcanism, contain both crystals and amorphous material. Crystallinity provides 33 information on the thermal history of the sample and is especially important in characterizing 34 volcanic rocks and pyroclasts because lava rheology is profoundly influenced by the crystal 35 content. Crystallinity is typically quantified via microscopy, using transmitted light or 36 backscattered electrons. However, many samples present visibly ambiguous textures such as 37 intimate intergrowth of crystal phases, and/or crystal sizes extending down to the nanometer 38 scale. Here we apply calorimetric methods involving heat capacity and enthalpy to assess the 39 crystallinity of a series of volcanic samples. We tested three different approaches, using 40 41 differential scanning calorimetry, on 30-40 mg aliquots of powdered basalts from the 2018 Kīlauea lower East Rift Zone. The first approach involves determining the magnitude of the 42 43 increase in heat capacity at the glass transition, which can determine crystallinity to a 1σ 44 precision of $\pm 3\%$. The second approach is based on the enthalpy of fusion, which requires a 45 longer more complex procedure with results that are typically more uncertain than for the heat capacity method, with a 1σ of $\pm 6\%$. A final method utilizing differences in enthalpies calculated 46 from the heat capacities required the most complex procedure, and has the greatest uncertainty of 47 ±18%. Preliminary results for lavas with microscopically determined crystallinities ranging from 48 49 11-98% indicate that crystallinity based on calorimetric data can be tens of percent higher than 50 the average value identified using microscopy and petrographic analysis. Image-based methodologies applied to sections of samples reveal spatial heterogeneity and details in texture 51 52 and crystallinity, whereas calorimetry-based methodologies capture the overall "bulk sample" 53 properties, unbiased by section effects or imaging resolution limits. These techniques are a powerful combination that can present complementary views of crystallinity. 54

55

56 57

58

59

KEYWORDS

Calorimetry; Crystallinity; Enthalpy; Heat Capacity; Lava Flows

61

60

62

INTRODUCTION

65	The crystal population of volcanic rocks and pyroclasts is an important characteristic for
66	reconstruction of magma history and eruption sequence (e.g. Mangan, 1990; Wall et al., 2014).
67	The degree of crystallinity and crystal size distributions record information about thermal history
68	(e.g. Marsh, 1981; Cashman & Marsh, 1988; Cashman et al., 1999; Simakin & Bindeman, 2008)
69	and exert strong controls over the rheology of the material (e.g. Dragoni & Tallarico, 1994;
70	Mader et al., 2013; Moitra & Gonnermann, 2015; Bain, 2021), which in turn feed back to ascent
71	rate and eruption style Cashman & Blundy, 2000; Popa et al., 2021). The crystallinity of lava and
72	tephra thus play important roles in the investigation of eruption dynamics, for both effusive and
73	explosive eruption products.
74	Examination of terrestrial volcanic materials is not the only application for crystallinity
75	characterization. Of interest to the wider community may be the calculation of crystallinity of
76	impact melts formed during bolide impacts on Earth and other bodies, and regolith on airless
77	bodies where frequent micro-impacts produce semi-crystalline agglutinates (e.g. Libourel et al.,
78	2022). Energy requirements for in situ resource utilization of regolith for extraterrestrial
79	construction via sintering or melting depend on its crystallinity (e.g. Meurisse et al., 2017;
80	Whittington & Parsapoor, 2022). Crystallinity is thus an important first-order property to
81	constrain for many geologic materials, terrestrial and planetary,
82	Crystal characteristics are typically explored using visual inspection methods, including
83	transmitted polarized light and backscattered electron (BSE) microscopy (e.g. Shand, 1927;
84	Reed, 1996; Higgins, 2006). However, many samples present visibly ambiguous textures such
85	as intimate intergrowth of crystal phases with interstitial glass, crystal sizes extending down to
86	the nanometer scale, and crystals that are indistinguishable from glass on the basis of average

atomic number. Crystallinity often cannot be accurately determined in such samples via microscopic inspection alone.

To constrain the crystal populations unable to be determined by the above-mentioned visual means, we propose the use of calorimetric and enthalpic methods. These are used routinely in the study of industrial glasses and polymers (e.g. Schick, 2009; Zheng *et al.*, 2019) and hold the potential to determine the crystallinity of volcanic samples as well. Calorimetric experiments can be run at the rate of one sample per 10-12 hours, depending on heating/cooling rates, and are capable of constraining all crystalline material regardless of size, intergrowth, or visual contrast, making them an attractive complement to point counting or thresholding-based methods of image analysis.

In this initial reconnaissance of calorimetric methods to determine crystallinity in volcanic materials, we have chosen a suite of well characterized lava samples from the fissure 8 and fissure 17 lava flows of the eruption of $K\bar{\imath}$ lauea in 2018. The samples span a wide range of crystallinity, from ~ 0 to $\sim 100\%$ at the mm-scale. We applied several calorimetric techniques, and traditional methods of microscopy at different scales, and compare the results, advantages, and disadvantages of the two approaches.

GEOLOGIC BACKGROUND

Kīlauea volcano on the island of Hawai'i began erupting along the lower East Rift Zone (LERZ) in early May of 2018. Twenty-four fissures opened up along the rift zone through the Leilani estates subdivision over the course of three weeks, starting on May 3rd (Neal *et al.*, 2019). These fissures were variably active and inactive through May, until activity narrowed to fissure 8

on May 28th (Neal et al., 2019). By mid-August, the lava flow field from fissure 8 had covered 108 35.5 km² and destroyed >700 homes (Williams *et al.*, 2020). 109 110 This eruption became the most thoroughly documented lava flow in history at that time. Hundreds of hours of drone footage (Desmither et al., 2021) and detailed on-the-ground 111 observations by the United States Geological Survey (USGS) and State personnel enabled the 112 collection of samples along the flow field emanating from the Ahu'ailā'au (formerly fissure 8) 113 114 cone, which range in both distance from the source vent, and eruptive date (Fig. 1). These samples record a variety of textures, with vesicularities from <5% to >80% and crystallinities 115 from <3% to nearly 100% (Fig. 2). 116 For several of the samples collected from fissure 8 flows, we found calculating total crystallinity 117 to be difficult by point-counting or image processing, whether from backscattered electron (BSE) 118 images acquired by scanning electron microscopy (SEM) or from polarized light images 119 120 acquired with a petrographic microscope. Two main obstacles restrict the ability to delineate crystal populations: 1) intergrowth or overlapping of crystals in thin sections causing the areas 121 surrounding large crystals to appear mostly opaque (Fig. 2a), and 2) fine, 'feathery' textures 122 123 suggesting incipient crystallization and the possibility of nanocrystals that are too small, and/or too finely intercalated with glass, to segment and evaluate using BSE imaging (Fig. 2b). These 124 textures and the range of total estimated crystallinities make this sample set well-suited to testing 125 126 the efficacy of several differential scanning calorimetry (DSC) methods for crystallinity calculation across a broad spectrum of crystal contents and sizes. 127

METHODOLOGICAL BACKGROUND

Heat capacity and enthalpy can be used to calculate bulk crystallinity via several different methods, all of which pertain to the thermodynamic transitions that occur upon heating and/or cooling of glassy and crystalline material. These transitions result in peaks and troughs in the measured heat capacity (C_p) of the samples at constant pressure, the integration of which results in the enthalpy (H):

129

130

131

132

133

134

135

136

137

138

139

140

141

142

143

144

145

146

147

148

$$dH = \int C_P dT$$
 Eq. 1

The enthalpy can contain both sensible and latent heat components, where latent heat is energy used for a phase transition, rather than for a temperature change. Differential scanning calorimetry allows for the separation of sensible and latent heat components, and the amount of latent heat released during crystallization or absorbed during melting is directly proportional to the fraction of material undergoing that phase transition, thus allowing determination of crystal or glass fraction. Application of the thermodynamic properties of heat capacity and enthalpy to calculations of crystallinity has been in use for around 60 years in polymer science (e.g. Dole, 1967; Mathot, 1984; Mathot & Pijpers, 1989; Kong & Hay, 2003; Jariyavidyanont et al., 2022). While the thermodynamic principles which govern crystallization and melting of materials are universal, polymers behave in ways that rocks and minerals do not. Polymers have a tendency to form two amorphous phases (Alsleben et al., 1991; Righetti et al., 2007; Schawe, 2017) and can occur as lamellae that shrink and grow with changing temperature (Höhne, 2002; Kong & Hay, 2003; Fosse et al., 2019). The first of these has no comparable analogy in geological materials, and while pyroxenes do form lamellae which may respond to temperature changes, this process is

much slower than timescales of calorimetric measurements, due to slow solid-state diffusion (Cherniak and Dimanov, 2010).

Conversely, polymers do not typically undergo 'cold crystallization' (e.g. Schawe, 2017; Fosse et al., 2019) where crystallization occurs after heating through the glass transition temperature (Tg) but while still below the liquidus, which is common for rock samples containing a mafic glassy component. Consequently, direct application of polymeric crystallinity calculations to rock samples would be difficult, as many methods used to quantify crystallization of polymers are specialized to those systems. The most useful method applicable to geological samples is that detailed in Mathot et al (1996), where a ratio of enthalpy differences between fully glassy, fully crystalline, and original sample is calculated to result in the crystallinity. We utilize this method as one of the three explored in this work.

Heat Capacity Curves

On initial heating, the heat capacity of crystalline materials increases with a concave-down curve that can be reproduced well with a 3- or 4-term Maier-Kelley equation (Richet & Bottinga, 1986; Robie & Hemingway, 1995). Rocks undergo melting over a range of temperatures, requiring an additional enthalpy of fusion that manifests as a peak in the heat capacity curve between the solidus and liquidus (Fig. 3a). Once molten, the heat capacity of the liquid is higher than that of the crystalline materials at the same temperature, and generally thought to be nearly independent of temperature (e.g. Stebbins *et al.*, 1984; Robert *et al.*, 2014; Hofmeister *et al.*, 2016; Mysen & Richet, 2019).

Glass Transition Temperature and Configurational Heat Capacity

Lava samples commonly contain a mixture of glass and crystals. Before ~600-700°C, the heat capacity curve is similar to that of fully crystalline or fully glassy material of the same composition (Fig. 3a), as crystalline and glassy materials of the same composition generally have similar heat capacities (Richet, 1984; Neuville & Richet, 1992; Robie & Hemingway, 1995; Mysen & Richet, 2019). Any glassy phases present will then encounter the glass transition temperature (Tg), above which they become a supercooled liquid, at a much lower temperature than the melting interval for crystalline materials (Fig. 3a vs. Fig. 3b). The glass transition for the glassy component of a partially crystalline lava may occur at a different temperature than seen in the fully remelted glassy sample, due to compositional differences. The glass transition usually occurs at higher temperatures for more evolved liquid compositions (Mysen & Richet, 2019). The increase in heat capacity, which results from heating through the glass transition, is known as the configurational heat capacity. It occurs as the energy of the system allows the molecules in the glass to explore new configurational states, becoming liquid (Richet & Bottinga, 1986). The magnitude of the configurational heat capacity rise scales linearly with the glass fraction in the starting material (Fig. 3b, Fig. 4a), with the height of the peak directly proportional to the amount of glass in the sample.

Crystallization Trough and Melting Peak

170

171

172

173

174

175

176

177

178

179

180

181

182

183

184

185

186

187

188

189

190

191

192

A supercooled liquid formed from glass being heated through the glass transition temperature is metastable and will commonly undergo partial to complete crystallization during continued heating (sometimes referred to as 'cold crystallization'). Crystallization is exothermic and will result in a trough in the measured C_P curve (Fig. 3b, 3c) as latent heat is released. Crystallization can be facilitated by the presence of pre-existing crystals providing growth sites, but the amount of crystallization is limited by the fraction of glass in the starting material. If this crystallization

is rapid relative to heating timescales, there may be a plateau after the trough at the crystalline heat capacity value. If crystallization is sluggish and incomplete, which is often the case for lavas, there may only be a slight inflection in the rising heat capacity curve between the crystallization trough and the melting peak, instead of a plateau (Fig. 3b vs. Fig. 3c).

On continued heating past the crystallization trough, should one exist, melting will be indicated by a peak in the heat capacity curve, corresponding to the latent heat of fusion. Any crystals grown during heating above the glass transition temperature melt quickly compared to phenocrysts inherited from the starting material, and it is common to see two or more peaks during melting, interpreted to represent crystal populations of different size and/or chemical composition (Fig. 3c). Using the size classification of Zellmer (2021), these are potentially (a) newly grown nano- and microlites (30 nm-1µm) formed in the calorimeter, (b) pre-existing microlites (~1-30 um) in the lava, and (c) phenocrysts of micro- and meso-cryst size (>30 um) in the lava (Fig. 3c).

Enthalpy from Heat Capacity Curves

Enthalpies of crystallization and fusion are calculated from the crystallization trough and melting peak by integration of those curves (Fig. 4a to Fig. 4b). The baseline of integration used when calculating the enthalpy of crystallization and fusion is sigmoidal, not linear, as there exists a transition between crystalline and fully liquid, where both exist in the system. The sigmoidal shape is drawn so that the inflection point occurs at the temperature of the minimum or maximum in the observed C_P curve, following the rate of crystallization or melting.

The enthalpies of fusion and crystallization are defined as the difference between the enthalpies of the solid, and liquid. (Fig. 4b) These are only equal if crystallization and fusion are measured

at the same temperature. Because crystallization occurs at a lower temperature than melting, and the heat capacity of the liquid is higher than that of the crystals, the enthalpy of crystallization measured in the calorimeter is always lower than the enthalpy of fusion (Fig. 4b). During heating of an initially partially crystalline sample, the observed enthalpy of crystallization will be smaller still. The different temperature ranges over which crystallization and melting occur for similar bulk compositions with different crystallinities or crystal-size distributions may also lead to some variation.

The evolution of sample enthalpy during heating can be quite complex (Fig. 4c). The precise shape of the curve depends on heating rate and the kinetics of melting and crystallization, which reflect bulk composition, grain size, and initial crystallinity. Using apparent heat capacity measurements, enthalpy can be tracked down-temperature from the liquidus for crystalline, glassy, and mixed materials. The enthalpy of the lava sample must lie between that of the fully crystalline and fully glassy starting materials, and its position will scale linearly with initial glass content.

METHODOLOGY

Sample Selection and Preparation

Five samples from along the fissure 8 lava flows were selected to span the range of possible crystallinities. Samples F8.17 and F8.20 are very glassy, while F8.8 and F8.11 are much more crystalline, with F8.18 falling in between. Approximately 60 grams of each sample was powdered, where possible from the same piece from which the thin sections used for validation were taken (F8.8, F8.11, F8.18). Where this was not possible, the samples appeared to be homogenous, and another similar piece was selected to be powdered (F8.17, F8.20). The

resultant powders were assumed to be a homogenous representative mixture, and 30-40 mg aliquots were utilized for each experiment.

Laboratory

237

238

239

240

241

242

243

244

245

246

247

248

249

250

251

252

253

254

255

256

257

258

Heat capacity measurements were collected using a Netzsch 404 Pegasus F1 Differential Scanning Calorimeter (DSC) with Pt-Furnace at the University of Texas at San Antonio (UTSA). Inert atmosphere was maintained through the experiments using a 30 ml/min Ar gas flow. Samples of ~30-40 mg mass were placed in Pt₉₀-Rh₁₀ pans with lids of a combined mass of ~260 mg (pans ~180 mg, lids ~80 mg). The pan weights tracked over the course of these experiments generally exhibit no detectable change using a balance precise to 0.01 mg, ensuring any iron loss from sample to the pans is negligible. Two pans were used: a reference pan, which remains empty, and a sample pan which contains reference materials or samples. For each sample measured in the DSC, three to four individual runs (herein a 'run' is a sequence composed of one heating leg and one cooling leg, with an intermediate plateau at high temperature) of the machine are needed: a baseline (laboratory file name designation 001), in which both the reference and sample pans are empty; a sapphire run (002), where an 84.5 mg sapphire disk is placed into the sample pan as a reference material; the sample run (003), in which 30-40 mg of the powdered sample replaces the sapphire disk; and a glass run (004), where the now-glassy sample previously melted in run (003) is remelted to generate a fully glass signal (Fig. 4a). The temperature program was the same for each run, starting with a heating ramp from 50 °C to 1500 °C at 30 °C/min, followed by a 10-minute dwell at 1500 °C to ensure thermal equilibration, and subsequent cooling back to 400 °C at 80 °C/min. The rapid cooling rate ensures quenching

of the sample to glass for the (004) glass run. The heating rate of 30 °C was chosen to be fast enough to produce strong signals and reduce experimental duration, and slow enough that thermal gradients within the sample would not be too large.

The heat flow (Q) between the sample pan and empty reference pan for each run is recorded in mW. Heat capacity is calculated from these readouts in the Netzsch™ Proteus software using the DIN 51007 method, a modification of the general heat flux equation solving for heat capacity:

$$C_P = \frac{Q}{m \times \dot{T}}$$
 Eq. 2

Where C_p is the heat capacity, m is the sample mass, and \dot{T} is the heating rate (K/min), which is constant for each run. In terms generated by the DSC, Eq. 2 becomes:

$$C_P = \frac{DSC - DSC_{baseline}}{m \times \dot{T}}$$
 Eq. 3

Where DSC and $DSC_{baseline}$ are the electrical signals recorded by the DSC in mW, m is the sample mass in mg, and \dot{T} is the heating/cooling rate in K/s.

In order to remove the effect of the Pt-Rh sample pan, the baseline (001) curve is subtracted from the three subsequent curves. The sample (003) and remelted sample (004) curves are then each ratioed against the reference sapphire (002) curve:

$$C_{P,sample} = \frac{DSC_{sample} - DSC_{baseline}}{DSC_{reference} - DSC_{baseline}} \times \frac{m_{reference}}{m_{sample}} \times C_{P,reference}$$
 Eq. 4

where $C_{P,sample}$ is the resultant heat capacity of either the original sample or glass, DSC_{sample} , 272 $DSC_{baseline}$, $DSC_{reference}$ are the values measured from the calorimeter for the original sample, 273 274 baseline, and reference (sapphire) respectively (see lines 003, 001, and 002 in Fig. 5(a)), m_{sample} and $m_{reference}$ are the masses of the original sample (and subsequent glass) and the reference 275 sapphire, and $C_{P,reference}$ is the known heat capacity of the reference sapphire. 276 Three distinct heat capacity curves are needed to determine crystallinity: a 100% glass 277 278 (holohyaline) curve, a 100% crystalline (holocrystalline) curve, and the original sample curve. 279 The first two provide known upper and lower bounds on crystallinity for the original. While the holohyaline and original sample runs can be collected in one day, the preparation of 280 281 the holocrystalline material requires more time. Crystallization experiments start by performing the baseline and sapphire runs with the usual temperature program. Next, the sample was held 282 for 48 hours at the temperature of the lowest point of the crystallization trough in the original 283 sample (003) run. At this temperature, glass has passed through T_g and begun to crystallize, but 284 has not yet begun to melt. 285 Once the long isothermal hold was completed, the crystalline sample was cooled to room 286 temperature and then runs (003) and (004) were performed as normal. Due to subsequent 287 288 melting of the crystallized holocrystalline material during these runs, their textures cannot be documented by petrographic analysis. However, examination of the heat capacity curves showed 289 290 no detectable glass transition for any experimentally crystallized sample. At the end of this 291 process, each sample was represented by C_P curves for the original material, holohyaline, and 292 holocrystalline equivalent.

Data Analysis

Using the heat capacity curves for the fully glassy, fully crystalline, and original sample, we explore three methods to estimate the original crystal content: 1) Configurational Heat Capacity Ratio (CHC), 2) Enthalpy Ratio (ER), and 3) Temperature Averaged Pre-Tg Enthalpy (TAPE). The essential steps for each method and their associated corrections are described here, with additional details described in the supplementary material.

The first and simplest method implemented is the configurational heat capacity (CHC) method. This method requires only the heat capacity curves for the original and holohyaline samples, and involves no corrections. Two pre- T_g heat capacity points are chosen by the user to act as 'baseline' values, one each for the original and holohyaline heat capacity curves (Fig. 6). Two more points are chosen at the highest point of the T_g peak for each curve. The difference between the two points for each curve is the configurational heat capacity for each curve.

The high point or peak seen at the start of the T_g rise in heat capacity is a kinetic feature, so we also calculated crystallinity using the plateau after this T_g peak instead. Comparison of the resultant crystallinities is discussed in the results and discussion. Once located, these four values are used to calculate the crystallinity, ϕ :

$$\phi (\%) = 100 * \left(I - \frac{Cp_{Original}^{Tg Peak} - Cp_{Original}^{Pre-Tg baseline}}{Cp_{Glass}^{Tg Peak} - Cp_{Glass}^{Pre-Tg baseline}} \right)$$
Eq. 5

where $Cp_{Original}^{Tg\ Peak}$ and $Cp_{Original}^{Pre-Tg\ baseline}$ are the points chosen for the Tg peak and pre-Tg baseline values, respectively, for the original sample curve, and $Cp_{Glass}^{Tg\ Peak}$ and $Cp_{Glass}^{Pre-Tg\ baseline}$ are the same for the holohyaline curve.

The second method is the enthalpy ratio (ER) method, which requires a correction factor to be applied to the enthalpy of crystallization values, to account for its temperature dependence (Eq.6 and 7; Fig. 4). All three heat capacity curves (original, holohyaline, and holocrystalline) are required for this method.

The first step of the ER method is to calculate the $\Delta H^{\text{crystallization}}$ and ΔH^{fusion} of each curve by integration of the crystallization trough and melting peaks. To prevent the temperature dependence of the enthalpies of crystallization and fusion (Fig. 4) from affecting the final crystallinity values, the $\Delta H^{\text{crystallization}}_{glass}$ and $\Delta H^{\text{fusion}}_{glass}$ are used to calculate a correction factor. Any crystalline material melted during the fusion peak in the glass heat capacity curve was generated during crystallization upon heating above Tg, so that the $\Delta H^{\text{crystallization}}_{glass}$ should equal the $\Delta H^{\text{fusion}}_{glass}$ (Fig. 7a). The ratio of these two values is used to calculate the correction

$$CF = \frac{\Delta H_{glass}^{fusion}}{\Delta H_{elss}^{crystallization}}$$
 Eq. 6

The correction factor is subsequently applied to the enthalpy of crystallization for the original sample to correct for the temperature difference between crystallization and melting. This corrected enthalpy of crystallization is subtracted from the enthalpy of fusion to remove enthalpy associated with crystals which formed from the glass component post-T_g. The adjusted enthalpy of fusion for the original sample is then divided by the enthalpy of fusion of the holocrystalline sample to calculate the original crystallinity:

factor (CF) for the temperature dependence of enthalpy:

$$\phi(\%) = 100 * \left(\frac{\Delta H_{original}^{fusion} - \left(CF * \Delta H_{original}^{crystallization} \right)}{\Delta H_{crystal}^{fusion}} \right)$$
Eq. 7

where $\Delta H_{original}^{fusion}$ and $\Delta H_{original}^{crystallization}$ are the enthalpy of fusion and crystallization, 330 respectively, for the original sample; and $\Delta H_{crystal}^{fusion}$ is the enthalpy of fusion of the 331 332 holocrystalline material. The third and final crystallinity calculation method explored in this work is the Temperature 333 334 Averaged Pre-T_g Enthalpy (TAPE) method. This method is applicable across geological and 335 polymer samples (Mathot et al., 1989), but is the most complicated and susceptible to large 336 uncertainties, due to multiple applied corrections. The first requirement of this method is that 337 heat capacities of the samples below T_g should be similar, so that any variations in calculated enthalpies below T_g will be minor. We found that this required heat capacity curves to be 338 339 adjusted vertically to a common pre-T_g baseline. We adjusted the holocrystalline and original 340 sample heat capacity curves to match the holohyaline curve, as this is normally the most stable of the curves below T_g (Fig. 8). 341 342 Once the heat capacity curves are aligned below T_g, the enthalpy values over the entire temperature range are calculated. This is most easily done by manually summing the apparent 343 heat capacity curves at 1 degree temperature intervals to generate enthalpy curves of H_T-H₃₂₈ for 344 345 each sample (original, holohyaline, holocrystalline), where H_T is the enthalpy of the sample at each temperature along the curve, and H_{328} is the enthalpy of the sample at room temperature 346

(Fig. 9).

The resultant curves each start at zero and diverge with increasing temperature (Fig. 9a). In order to calculate the actual enthalpy difference between samples, the curves must be anchored at a known reference point where they are all in the same state. The best choice is the highest liquidus temperature measured among the three runs, which is typically for the holocrystalline sample. Having selected a liquidus temperature, the other relative enthalpy curves are adjusted up until all three curves meet at this anchor point. At lower temperatures, the holocrystalline sample should always have the lowest enthalpy of the three runs. The graph now shows enthalpy relative to that of the holocrystalline sample at the starting temperature (Fig. 9b).

$$\phi = 100 \times \left(\frac{\Delta H_{glass} - \Delta H_{original}}{\Delta H_{glass} - \Delta H_{crystal}} \right)$$
 Eq. 8

where ΔH_{glass} , $\Delta H_{original}$, and $\Delta H_{crystal}$ are the enthalpies relative to the holocrystalline sample at room temperature, i.e. the values plotted in Figure 9b. We calculated the crystallinity at each temperature step over a range pre-T_g, typically between 250 °C and 600 °C, and took the average (Fig. 10).

VALIDATION: CRYSTALLINITY BY IMAGE ANALYSIS

Crystallinities via petrography

between the enthalpies:

Traditional petrography provides a basis for independently assessing the crystallinity values obtained by DSC methods. Crystallinity values were obtained by analyzing electron imagery, including backscatter electron (BSE) images and wavelength dispersive spectroscopy (WDS) X-ray element intensity maps, acquired on splits of the same five fissure 8 lava samples. Qualitative

X-ray intensity maps were acquired using the University of Hawai'i at Mānoa's JEOL JXA-8500F field emission electron microprobe. Backscattered electron images were collected on the JXA-8500F microprobe and the FEI Helios NanoLab 660 Dual Beam FIB-SEM, both situated in the School of Ocean and Earth Science and Technology at the University of Hawai'i at Mānoa. Preliminary BSE imaging surveys of the samples revealed crystallinity variation from 0 to 100% over the scale of mm (samples F8.11 and F8.18 being particularly heterogeneous), with crystal length scales ranging from sub-micron to several mm (Fig. 11). Relative to typical volcanic scoria or pumice, the fissure 8 lava samples preserve an exceptionally high degree of spatial heterogeneity. The large range of relevant spatial scales required the development of a tailored approach so as to representatively assess crystallinities of full thin sections on a practical time frame.

Traditional petrographic methods including point counting and pixel thresholding were integrated and modified to incorporate electron microscopy (EM) imaging techniques. The workflow is summarized in Figure 12, with additional details provided in the Supplement.

Characterization at the thin-section scale: WDS maps

At the coarsest scale, full-section X-ray intensity maps acquired with the electron microprobe's wavelength-dispersive spectrometers (WDS) were used to evaluate the abundances of phenocrysts and mesocrysts of olivine, Ca-clinopyroxene, feldspar, and Fe-Ti oxides. Elemental intensity maps of Al, Mg, and Ca are combined into a single RGB image, from which we obtain the dense-rock normalized abundances of olivine, feldspar, and Ca-clinopyroxene crystals greater than ~50 μm equivalent diameter (Fig. 12 a-e). The phase maps (Fig. 12 f and g) were subsequently processed to obtain information in two crystal size bins: mesocrysts (50-150 um)

and phenocrysts (>150 um). This was achieved using ImageJ software to mathematically erode binary images created for each phase by thresholding the phase maps. The difference between the original phase abundance and the post-erosion phase abundance yields the area percentage of mesocrysts.

Characterization at the sub-mm scale: BSE image nests

The abundances of microlites (<50 um) are obtained by representative sub-sampling of the petrographic thin sections with BSE imaging. Images are collected at randomly selected locations, distributed evenly across each thin section (typically >30 images per sample; Fig. 121). Polyhedral microlites of feldspar and clinopyroxene are comparatively easy to identify at the lower-magnifications (200x-500x) and are amenable to abundance determination by simple point-counting. However, discerning finer intergrowths and evaluating the abundance of glass required magnification >1000x, at which scale it is not possible to capture the coarser microlites representatively. The point counting technique was modified to address this difficulty. Highmagnification images were used to (a) define microtextural domain types and (b) determine phase abundances in each type. Lower-magnification images were used to carry out the point counting, with grid intersections allocated to individual phases as well as domain types (Fig. 12m). The fine-grained domains were parsed to the appropriate phase tallies in an offline calculation. The resultant crystallinities and the uncertainties inherent in the analytical techniques, as well as due to sample heterogeneity, are recorded in Table 1. See the Supplement for additional details.

RESULTS

390

391

392

393

394

395

396

397

398

399

400

401

402

403

404

405

406

407

408

409

411 All three calorimetric calculations were successfully applied to the five basalt samples, with

varying degrees of precision. The CHC method provided the best overall agreement to the

413 WDS/BSE crystallinities (Fig. 13).

- The values calculated for this method, using the peak of the glass transition curve, fall neatly
- within the 1σ uncertainties for the BSE/WDS calculations for those samples with little
- heterogeneity (Fig. 13). For samples F8.11 and F8.18 with high heterogeneity, the CHC peak
- values (82 \pm 3 % and 64 \pm 3 %, respectively) fall within the maximum and minimum (69-109 %
- and 13-68 %, respectively, the variation due to sample heterogeneity) crystallinity values found
- using BSE/WDS for those samples. Their location within this range is a reflection of the mixing
- and homogenization of the crystal-poor and crystal-rich domains during powdering. CHC
- calculations using the plateau of the T_g peak result in more variable answers, plotting well
- outside of the uncertainties for the glassiest samples, but falling closer to the average for F8.18.
- Even when used on the very ambiguous 'peaks' of T_g for the two most crystalline samples, F8.8
- and F8.11, the resultant CHC peak crystallinities ($97 \pm 3\%$ and $82 \pm 3\%$, respectively) fit well
- with the analytical uncertainty of the BSE/WDS values ($98 \pm 4\%$ and $89 \pm 4\%$, respectively).
- Given the poorly defined T_g peak, this was not expected, but it appears that the CHC method
- may work well even at very low glass contents.
- Of the two enthalpy methods, the ER method matches most closely the BSE/WDS calculations,
- with most points falling within the BSE/WDS sample heterogeneity uncertainties (Fig. 14).
- Only the F8.18 values are not well constrained (83 \pm 6%, well outside the BSE/WDS values of
- 431 $40 \pm 28\%$) and this is due to the sample itself rather than the method (see discussion).
- The TAPE method results in four of the five samples overlapping with the BSE/WDS values.
- However, this is only due to the large uncertainties on the TAPE values. The uncertainty on these

values is \sim 3 times that of the uncertainty of the ER method, and 6 times that of the CHC method, with the maximum uncertainty on these values at \pm 18%. All crystallinity values and their uncertainties are recorded in Table 2.

Application to texturally ambiguous samples

434

435

436

437

438

439

440

441

442

443

444

445

446

447

448

449

450

451

452

453

454

455

456

Validation of the three calorimetric methods has now been established on samples with a wide range of crystallinities, using the highly detailed BSE/WDS crystallinity determination. To demonstrate the power of these methods for samples with indeterminable groundmass, we present image-thresholding comparisons of three samples from the fissure 17 flow of the Kīlauea lower East Rift Zone eruption of 2018 (Fig. 1). The material erupted from the fissure 17 vent was notable for its initial icelandite composition (a high-iron, aluminum-poor andesite; Carmichael, 1964; Carmichael et al., 1974), and more explosive eruption style, in contrast to the basalt characterizing the rest of the eruption. The two basalts and one icelandite sample characterized here show a variety of intergrowth and microlitic textures, with little to no visible glass, and large areas (>40% of the total area) that remain visibly ambiguous in a petrographic microscope (Fig. 2a). Crystallinities and bubble contents were determined using color-image thresholding of full thin section plane-polarized light images collected via petrographic microscopy (Fig. 2a). Individual regions of interest (ROI) were delineated using distinct color differences between bubbles (containing blue epoxy), crystals large enough to be intersected on both sides of the thin section (white/grey) and ambiguous groundmass (brown/black). Crystallinity was calculated by dividing the selected crystal pixel number by the combined value of selected crystals and groundmass. Groundmass contents were first estimated by direct selection, and secondly by subtracting pixels classified as crystals or bubbles from the total number of pixels in the image. The resulting

crystallinity estimates were often quite different to each other (Table 2). Due to the opacity of the groundmass, its crystallinity could not be determined, so that the crystallinities calculated by petrography are minimum estimates, with a maximum possible crystallinity of 100%. For the fissure 17 samples, the CHC crystallinity is in good agreement with the ER crystallinity in two of the samples, while the ER crystallinity is markedly higher in F17-10. The TAPE crystallinity is much more variable than the other two methods, as also noted for the fissure 8 samples, with a low estimate for F17-07, and an extremely high crystallinity for F17-08B. However, the TAPE method matches well with the CHC crystallinity calculated for F17-10, while the ER crystallinity is high. While the two basalt samples show a marked increase in the precision of crystallinity using the calorimetric methods, the icelandite, F17-10, shows fairly good agreement between the image thresholding values and the calorimetric methods. This is most likely due to the appearance of iron-rich nano- and microlites in the basalts, causing complete opacity of the groundmass. In contrast, the icelandite appears to be more translucent, allowing the delineation of some crystals

DISCUSSION

within (see Supplement).

457

458

459

460

461

462

463

464

465

466

467

468

469

470

471

472

473

474

475

476

477

478

Uncertainty Propagation of Crystallinity Calculations

The prime source of uncertainty for all three methods comes in the form of human error, due to the wide range of values that rely on the user to pick them from a graph, and so are subject to observational differences. In order to quantify these, it is important to encapsulate the possible areas of human error in the uncertainty propagation for these methods. We calculated the 1σ uncertainty on three different samples, with varying degrees of glassiness, and DSC curve

clarity. These three samples were F8.17 (very glassy, near perfect curves), F8.8 (very crystalline, fairly well defined curves), and F17-07 (a glassy/crystalline mix of icelandite composition with very poor curves).

The CHC method has only one main source of uncertainty, from the choice of baseline and peak/plateau values for the glass transition. To calculate uncertainty, each of these points was determined 5 times each by 3 separate individuals, and the resulting standard deviation was taken as the uncertainty for those values. The CHC method using the plateau results in F8.17, F8.8, and F17-07 1σ uncertainties of 1%, 0.6%, and 2%, while utilizing the peak results in 0.8%, 0.4%, and 2%, respectively. We took the highest of these three values to be the uncertainty for all samples.

The two enthalpy methods required at least one correction or anchoring step, which impart higher uncertainties. The main source of uncertainty for the ER method lies in the choices of upper and lower temperature bounds for the enthalpy of crystallization and enthalpy of fusion calculations. To constrain this uncertainty, the upper and lower bounds used to calculate enthalpy from the crystallization trough and melting peak were chosen five times each by three separate individuals, for each curve. The standard deviation of the resultant enthalpies was used as the uncertainty for each enthalpy value. Propagation of the uncertainties through the equation resulted in $\pm 3\%$, $\pm 1\%$, and $\pm 6\%$ 1 σ uncertainty for F8.17, F8.8, and F17-07, respectively. As with the other methods, we quote the largest of these as the overall uncertainty of the method. The TAPE method requires multiple adjustments, each of which introduces additional

The TAPE method requires multiple adjustments, each of which introduces additional uncertainty. The first is the baseline C_P correction, which shifts all of the heat capacity curves to the same average values below T_g. All of the samples except for F8.17 required this adjustment. Next is the enthalpy adjustment, to anchor all curves at the same enthalpy value at or above the

liquidus temperature. At times, it was necessary to choose between two possible anchoring values, either because the heat capacity curves converged at more than one location post-melting, or the completion of melting was ambiguous. Most possible ambiguity is due to inclusion or exclusion of a final long, low melting peak which can be overlooked, but which we attribute to slower melting of larger crystals (see Supplement F8.17 heat capacity data). Full explanation of these choices is provided in the supplementary material. Propagating uncertainties from these two adjustments results in 1σ uncertainties of 0.3%, 18%, and 12% for F8.17, F8.8, and F17-07 respectively. The low uncertainty for F8.17 results from lack of the heat capacity correction.

Caveats and considerations for the WDS/EDS Methodologies

The determination of crystallinity at the full-section scale with WDS maps is essentially a thresholding technique, and thus presents several advantages as well as important caveats and limitations. As compared with manual feature segmentation, the technique is not labor intensive. It is therefore relatively quick to apply and the outcome is relatively insensitive to operator bias. On the other hand, no information is obtained about feature shape, individual feature size, or the spatial distribution of the phases. The pixel size of our WDS maps is 24.5 µm. Given the relatively unlikely chance that a similar-sized crystal will be perfectly centered on a pixel, there is an effective minimum detection size influenced by several factors: (a) the actual position of the phase with respect to the pixel-grid and thus the likelihood that many pixels represent 'mixed analyses'; (b) the elemental contrast of the phase with respect to its surroundings (with comparison to basaltic glass, this contrast is generally greatest for olivine, and less for feldspar and least for Ca-cpx); (c) the absolute signal strength (concentration) of Al, Mg, or Ca in each phase (again, greatest for Mg in olivine). Close comparison of WDS maps with high-

magnification BSE images supports our estimate that 50 μ m (equivalent diameter) is the minimum detection size limit with this technique.

Finally, as with any sectioning approach, the characterization of a randomly-chosen 2D surface within the bulk rock may not be representative of the whole specimen, particularly in samples that have steep texture gradients caused by variable cooling rate at the margin of a lava sample. For example, the proportion of a 3D sample that is glassy rind may differ from the proportion contained within its corresponding 2D section, giving rise to substantial differences in crystallinity. Such discrepancies are not limitations of the analytical techniques, insofar as the technique accurately recovers the proportions present in the two sample types, but rather a limitation of the implied assumption of a section's representativeness.

While computed tomography and similar instrumentation has proved useful in classifying crystallinity in three-dimensions (e.g. Baker et al, 2012), this works primarily for large, high-density-contrast crystals. These methods would run into the same issues mentioned previously for the two-dimensional methods in the samples studied here: complex crystal textures, nano-and micro-scale crystallinity, and small volume characterization. As such, while three-dimensional methods enable calculation of vol. % crystallinity of certain phases, these techniques would still benefit from utilization of the techniques presented here to ensure wholescale crystallinity capture, especially in samples with complex textures, and similar-density crystal phases.

Caveats and considerations for the enthalpy-based techniques

The ER and TAPE methods both require heat capacity data for holocrystalline samples. For two samples (F8.8 and F8.17) the holocrystalline curve used for calculations was obtained from a

sample held at the isotherm for 1 hour rather than the 48 hours proposed as a standard method. This is because we sometimes observed inconsistencies in the measurements on samples crystallized for 48 hours, which resulted in enthalpies of fusion that were lower than those of the original sample. For sample F8.18, we created six separate holocrystalline runs, only one of which resulted in an enthalpy of fusion greater than any of the three separate original sample runs. F8.18 appears to be the most heterogeneous of all our samples, which may account for some of this variation. Should large portions of one crystal phase be available in any particular aliquot, the melt chemistry and crystal chemistry may be markedly different, producing variation in the enthalpies of fusion. It is unclear why F8.8 and F8.17 had larger enthalpies of fusion for shorter isothermal holds, as they are both much more homogeneous in bulk texture.

The second point of consideration is that of the temperature at which the isothermal holds are carried out. During the six separate 48 hour isothermal holds done on sample F8.18 aliquots, we varied the temperature between the starting and ending temperatures of the crystallization trough in order to discern if that may have an effect. While no definitive conclusion was reached, choosing a temperature below the base of the crystallization trough, and above the first inflection point of this trough, should ensure that the sample is kept below its solidus, and that there is sufficiently rapid crystallization to ensure crystal nucleation and growth. This will become more difficult in more silicic samples, where crystallization kinetics are slower (e.g. Hammer, 2008). An additional consideration for more silicic samples is a degassing signal due to higher water content, which may cause an anomalous increase in the Tg peak as the sample degasses immediately following Tg.

A final consideration is that of dimensionality, as the calorimetry methods result in wt % crystallinity, while the two-dimensional image thresholding methods result in area %

crystallinity. However, the two should be approximately equivalent due to the low difference in densities between the various crystal phases and glass in the samples.

Which methods should I use?

569

570

571

572

573

574

575

576

577

578

579

580

581

582

583

584

585

586

587

588

589

590

Of the three calorimetric methods explored here, the CHC method appears to be the most precise when compared to the BSE/WDS values. Within this method, two approaches were explored, using either the peak or plateau of the glass transition curve as the high point for the calculation. The CHC calculations using the T_g peak all resulted in values which overlapped well within the 1σ uncertainty of the BSE/WDS calculations, while this proved true for only some of those calculated using the plateau (Fig. 13). The uncertainties calculated for both CHC approaches were the lowest of any of the three calorimetric methods, with a maximum 1σ uncertainty of 3%. This method is also the fastest and easiest to apply of the three methods explored in this work. It requires only the original and holohyaline in the DSC, removing the need for the creation of a holocrystalline sample, and in so doing shortening the data collection time to a day. The calculation itself has only three steps and requires no corrections. Second to the CHC method is the ER method, which also resulted in calculated crystallinities which fall within the uncertainty bounds of the BSE/WDS crystallinities, except for F8.18 (Fig. 14). This sample has the largest internal heterogeneity, which is the likely driver for the disparate values calculated by all methods. The ER method does require a holocrystalline sample to be measured in the DSC, adding at least 48 hours onto the collection time. The calculation of crystallinity is a simple ratio once the temperature-dependence correction factor is applied. This method thus requires more time and effort than the CHC method, but produces acceptable results on homogeneous samples.

The TAPE method is the most complex and least precise method of the three explored in this work. While four of the five sample crystallinities calculated fell within the 1σ uncertainty of the BSE/WDS crystallinity calculations, this is primarily due to the large $\pm 18\%$ 1σ uncertainty on the TAPE crystallinity values themselves (Fig. 15). This uncertainty is three times the maximum uncertainty on the ER crystallinities, and six times that of the CHC method. When applied to the three fissure 17 samples, this method resulted in discrepancies relative to the other two calculations, one at least that gave an impossible calculated value of greater than 100% crystallinity. This appears to be largely due to a baseline tilt in the enthalpy curve of the original sample, which results in the low-temperature end of the curve becoming negative when anchoring is applied. As such, baselines must be exceptionally flat and reproducible to get reliable results using the TAPE method. Finally, this method requires an additional 48-hour isothermal period to attain a holocrystalline sample, and for multiple corrections and assumptions to be applied when calculating the crystallinity.

In summary, uncertainties in total crystallinity are typically lower for calorimetric methods than petrographic methods, partly due to the ability to detect nanoscale ordering or lack thereof, and in part due to textural domain averaging by powdering in creating a bulk sample. Conversely, petrographic methods have an advantage in that they can preserve textural information such as crystal size and shape distribution. We conclude that the two techniques are complementary and provide a powerful combined approach.

Future directions - Crystal Size Populations

The DSC curves of several samples contain more than one peak during melting. We postulate that this is due to different crystal size populations in the sample. This is supported by several indications: (1) Samples which initially contained a significant amount of glass showed an

additional melting peak just higher in temperature than the crystallization trough during the original run. This feature was not visible in the C_P curve from the holocrystalline sample (i.e. Fig. 8). The only difference between these curves is the glass found in the original sample, which crystallized nano-to-microlites during heating post T_g. (2) Long low peaks at the end of melting which are visible only in those samples we know contain phenocrysts, and are not present in the holohyaline run. During heating, larger crystals take longer to melt completely, and thus seem to incorporate latent heat of fusion at higher temperatures than smaller crystals. Additionally, the holohyaline run is devoid of these high temperature features, and does not contain any larger crystals, which cannot grow on the experimental timescales used here. In summary, it is possible to discern at least rough crystal size populations from the details of the fusion peak. Depending on the presence of glass, samples may include a very small sharp peak on the front of the 'main' melting peak, which indicates the presence of nanolites and/or microlites, grown post-Tg. If no glass is present, and such a peak occurs, it is likely the sample contains naturally occurring nanolites/small microlites. The middle peak, or main peak of melting, is conjectured to indicate the presence of large microlites and small phenocrysts, while a long, low peak usually seen after inflection point of this main peak indicates larger phenocrysts, likely pre-eruptive in the case of quenched basaltic lavas. The areas under these individual peaks could, in theory, be used to calculate the relative masses of different size populations. As mentioned previously, this line of inquiry would require detailed sample determination, as large crystal heterogeneity in the samples could result in aliquots with highly variable large vs. small crystal contents. Additional care would need to be taken when creating the powdered sample, so as not to break apart crystals, and thus mechanically modify the resultant calculated crystal size distribution.

614

615

616

617

618

619

620

621

622

623

624

625

626

627

628

629

630

631

632

633

634

635

CONCLUSION

We have investigated three methods for the calculation of crystallinity from calorimetric data, for samples ranging from single-digit to near 100% crystallinities. Of these three methods, we propose that the CHC calculation is the easiest, fastest, and most accurate method (±3 vol.% crystals), even for those samples which have very poorly defined Tg peaks. For highly crystalline samples where the Tg peak may be very hard to quantify, we additionally recommend the enthalpy ratio method, as it requires fewer additional measurements and less processing than the TAPE method. Petrographic methods have an advantage in that they can preserve textural information such as crystal size and shape distribution, but the example of the fissure 17 samples with opaque, very fine-grained (i.e. sub-micron scale) mesostasis underscores the ability of calorimetric data to provide textural information that is difficult or impossible to quantify with optical or electron microscopy. We conclude that the two techniques are complementary and provide a powerful combined approach to the study of lavas and other rocks containing an amorphous phase.

ACKNOWLEDGEMENTS

This work was supported by NSF EAR 1928923 to AW and NSF EAR 1929119 to JH. BH, AE and AW were also supported by the NASA MIRO Center for Advanced Measurements in Extreme Environments, Grant 80NSSC19M019. We gratefully acknowledge assistance in the field from Brett Carr, Hannah Dietterich, John Dye, Carolyn Parcheta, Matt Patrick, and Mike Zoeller. We thank the Leilani Estates neighborhood association and several individual landowners for access to their property and permission to sample.

659 **REFERENCES**

- Alsleben, M., et al (1991) Determination of peak base line for semicrystalline polymers.
- 661 *Thermochimica Acta* 187, 261-268
- Bain, A., et al. (2021) Micro-textural controls on magma rheology and vulcanian explosion
- 663 cyclicity. Frontiers in Earth Science 8.
- Baker, D. R., et al. (2012). An introduction to the application of X-ray microtomography to
- the three-dimensional study of igneous rocks. *Lithos*, 148, 262-276.
- Blundell, D. J., et al. (1981). Routine crystallinity measurements of polymers by d.s.c. *Polymer*
- 667 22(5), 704–707.
- Blundy, J. & Cashman, K.V. (2008) Petrologic reconstruction of magmatic system variables and
- processes. Reviews in Mineralogy and Geochemistry 69, 179-239.
- 670 Carmichael, I. (1964) The petrology of Thingmuli, a Tertiary volcano in eastern Iceland. *Journal*
- 671 *of Petrology* 5, 435–460
- 672 Carmichael I., et al. (1974) *Igneous petrology*. McGraw-Hill Book Co., New York
- 673 Cashman, K.V., et al. (1999) Cooling and crystallization of lava in open channels, and the
- transition of Pāhoehoe Lava to 'Ā'a. *Bulletin of Volcanology* 61, 306-323
- 675 Cashman, K.V. & Blundy, J. (2000) Degassing and Crystallization of Ascending andesite and
- dacite. Philosophical Transactions: Mathematical, Physical and Engineering Sciences
- 677 358(1770), 1487–513.
- 678 Cashman, K., and Marsh, B. (1988) Crystal Size Distribution (CSD) in rocks and the kinetics and
- 679 dynamics of crystallization .2. Makaopuhi lava lake. Contributions to Mineralogy and Petrology
- 680 99, 292–305. doi: 10.1007/bf00375363
- 681 Cherniak, D.J. & Dimanov, A. (2010) Diffusion in Pyroxenes, Mica, and Amphibole. Reviews in
- 682 Mineralogy and Geochemistry, 72, 641-690, doi: 10.2138/rmg.2010.72.14.
- Desmither, L., et al (2021). Unoccupied Aircraft Systems (UAS) video of the 2018 lower East
- Rift Zone eruption of Kīlauea Volcano, Hawai'i. Volcano Science Center Data Release.
- Dietterich, H., et al (2021) Lava effusion rate evolution and erupted volume during the 2018
- Kilauea lower East Rift Zone eruption. Bulletin of Volcanology, 83:25
- Dragoni, M. & Tallarico, A. (1994) The effect of crystallization on the rheology and dynamics of
- lava flows. *Journal of Volcanology and Geothermal Research* 59(3), 241-252.

- Dole, M. (1967) Crystallinity from Thermal Measurements. *Journal of Polymer Science*, *Part*
- 690 *C*(18), 57–68.
- Fosse, C., et al. (2019). Determination of the equilibrium enthalpy of melting of two-phase semi-
- 692 crystalline polymers by fast scanning calorimetry. *Thermochimica Acta* 677, 67–78.
- 693 Gray, A.P. (1970). Polymer Crystallinity Determinations By DSC*. *Thermochimica Acta* 563.
- Hammer, J.E. (2008) Experimental studies of the kinetics and energetics of magma
- 695 crystallization. Reviews in Mineralogy & Geochemistry 69, 9-59.
- 696 Higgins, M. (2006) Textural Measurements in Igneous and Metamorphic Petrology. Cambridge
- 697 University Press.
- Hofmeister, A.M., et al. (2016) Transport properties of glassy and molten lavas as a function of
- temperature and composition. Journal of Volcanology and Geothermal Research 327, 330-348
- Höhne, G. W. H. (2002) Another approach to the Gibbs-Thomson equation and the melting point
- of polymers and oligomers. *Polymer* 43(17), 4689-4698
- Jariyavidyanont, K., et al (2022). The bulk enthalpy of melting of α'-crystals of poly (L-lactic
- acid) determined by fast scanning chip calorimetry. *Thermochimica Acta*, 717.
- 704 https://doi.org/10.1016/J.TCA.2022.179349
- Kong, Y., & Hay, J. N. (2003). The enthalpy of fusion and degree of crystallinity of polymers as
- measured by DSC. European Polymer Journal, 39(8), 1721–1727.
- 707 https://doi.org/10.1016/S0014-3057(03)00054-5
- 708 Libourel, G., et al (2022) Non-terrestrial melts, magmas, and glasses. Reviews in Mineralogy and
- 709 *Geochemistry* 87(1), 887-918.
- Mader, H., et al (2013) The rheology of two-phase magmas: A review and analysis. *Journal of*
- 711 *Volcanology and Geothermal Research 257*, 135-158.
- 712 Mangan, M. (1990) Crystal size distribution systematics and the determination of magma storage
- 713 times: The 1959 eruption of Kīlauea volcano, Hawai'i. *Journal of Volcanology and Geothermal*
- 714 Research, 44(3-4), 295-302.
- Marsh, B.D. (1981) On the crystallinity, probability of occurrence, and rheology of lava and
- magma. *Contributions to Mineralogy and Petrology* 78, 85-98.
- Mathot, V. B. F. (1984). Temperature dependence of some thermo-dynamic functions for
- amorphous and semi-crystalline polymers. *Polymer*, 25(5), 579–599.
- 719 https://doi.org/10.1016/0032-3861(84)90025-9

- 720 Mathot, V. B. F., & Pijpers, M. F. J. (1989). Heat capacity, enthalpy and crystallinity of
- 721 polymers from DSC measurements and determination of the DSC peak base line.
- 722 Thermochimica Acta 151(C), 241–259. https://doi.org/10.1016/0040-6031(89)85354-7
- Mathot, V., et al (1996) Dynamic DSC, SAXS and WAXS on homogeneous ethylene-propylene
- and ethylenf~octene copolymers with high comonomer contents. *Journal of Thermal Analysis*
- 725 46, 681-718.
- Meurisse, A., et. al. (2017) Influence of Mineral Composition on Sintering Lunar Regolith.
- *Journal of Aerospace Engineering* 30, 04017014. DOI:10.1061/(ASCE)AS.1943-5525.0000721
- Moitra, P. & Gonnermann, H. (2015) Effects of crystal shape- and size-modality on magma
- 729 rheology. Geochemistry, Geophysics, Geosystems 16(1), 1-26.
- 730 Mysen, B.O., & Richet, P. (2019) Silicate Melts and Glasses (2nd Edition). Elsevier.
- Neal, C.A., et al. (2019) The 2018 rift eruption and summit collapse of Kīlauea Volcano.
- 732 *Science*, 363 (6425), 367-374.
- Neuville, D. R. & Richet, P. (1992) Thermodynamics of Silicate Melts: Configurational
- Properties. In: Saxena, S.K. (ed) *Thermodynamic Data*, Springer-Verlag New York Inc.
- Popa, R., et al (2021) Explosive or effusive style of volcanic eruption determined by magma
- storage conditions. *Nature Geoscience* 14(10), 781-786
- Reed, S.J.B., (1996) *Electron Microprobe Analysis and Scanning Electron Microscopy in*
- 738 *Geology*. Cambridge: Cambridge University Press.
- Richet, P. (1984) Viscosity and configurational entropy of silicate melts. *Geochimica et*
- 740 *Cosmochimica Acta*, 48(3), 471-483.
- Richet, P. & Bottinga, Y. (1986) Thermochemical properties of silicate glasses and liquids: A
- review. Reviews of Geophysics, 24(1), 1-25.
- Righetti, M., et al. (2007) Enthalpy-based determination of crystalline, mobile amorphous, and
- ridged amorphous fractions in semicrystalline polymers Poly(ethylene terephthalate).
- 745 *Thermochimica Acta*, 462(1-2), 15-24.
- Robert, G., et al. (2014) Heat capacity of hydrous basaltic glasses and liquids. Journal of Non-
- 747 *Crystalline Solids* 390, 19-30. doi: 10.1016/j.jnoncrysol.2014.02.011
- Robie, R. A. & Hemingway, B. S. (1995). Thermodynamic properties of minerals and related
- substances at 298.15 K and 1 bar (105 pascals) pressure and at higher temperature. U.S.
- 750 Geological Survey Bulletin 2131, 470.

- Schawe, J. E. K. (2017). Remarks regarding the determination of the initial crystallinity by
- 752 temperature modulated DSC. *Thermochimica Acta* 657, 151–155.
- 753 <u>https://doi.org/10.1016/J.TCA.2017.09.006</u>
- Schick, C. (2009) Differential scanning calorimetry (DSC) of semicrystalline polymers.
- 755 Analytical and Bioanalytical Chemistry, 395, 1589-1611.
- Shand, S.J. (1927) Eruptive Rocks: their Genesis, Composition, Classification, and their
- 757 Relation to Ore-Deposits; with a Chapter on Meteorites. London: Thomas Murby and CO., New
- 758 York: D. Van Nostrand Co. 360.
- 759 Simakin, A.G. & Bindeman, I.N. (2008) Evolution of crystal sizes in the series of dissolution and
- 760 precipitation events in open magma systems. Journal of Volcanology and Geothermal Research
- 761 177, 997–1010.
- Stebbins, J.F., et al. (1984) Heat capacities and entropies of silicate liquids and glasses. *Contrib*.
- 763 *Mineral. Petrol.*, 86: 131-148.
- Wall, et al. (2014) Determining volcanic eruption styles on Earth and Mars from crystallinity
- measurements. *Nature Communications* 5.
- 766 Whittington, A. & Parsapoor, A., (2022) Lower Cost Lunar Bricks: Energetics of Melting and
- Sintering Lunar Regolith Simulants. New Space, 10. doi:10.1089/space.2021.0055
- Williams, D. M., et al. (2020) U.S. Geological Survey 2018 Kīlauea Volcano Eruption Response
- in Hawai'i After-Action Review. U.S. Geological Survey Open-File Report 2020-1041, 56p.,
- 770 <u>https://doi.org/10.3133/ofr20201041</u>
- 771 Zellmer, G.F. (2021) Gaining acuity on crystal terminology in volcanic rocks. *Bulletin of*
- 772 *Volcanology* 83, 78, https://doi.org/10.1007/s00445-021-01505-9
- 773 Zheng, Q., et al (2019) Understanding Glass through Differential Scanning Calorimetry. *Chem.*
- 774 Rev. 119(13), 7848-7939.
- Zoeller, M.H., et al (2020) Geospatial database of the 2018 lower East Rift Zone eruption of
- 776 Kīlauea Volcano, Hawai'i: U.S. Geological Survey data release,
- 777 https://doi.org/10.5066/P9S7UQKQ.

Figure Captions

Figure 1: Flow depth map of fissure 8 and fissure 17 flows of the Kīlauea lower East Rift Zone eruption. Sample locations are shown as red triangles. Modified from Dietterich *et al.* (2021).

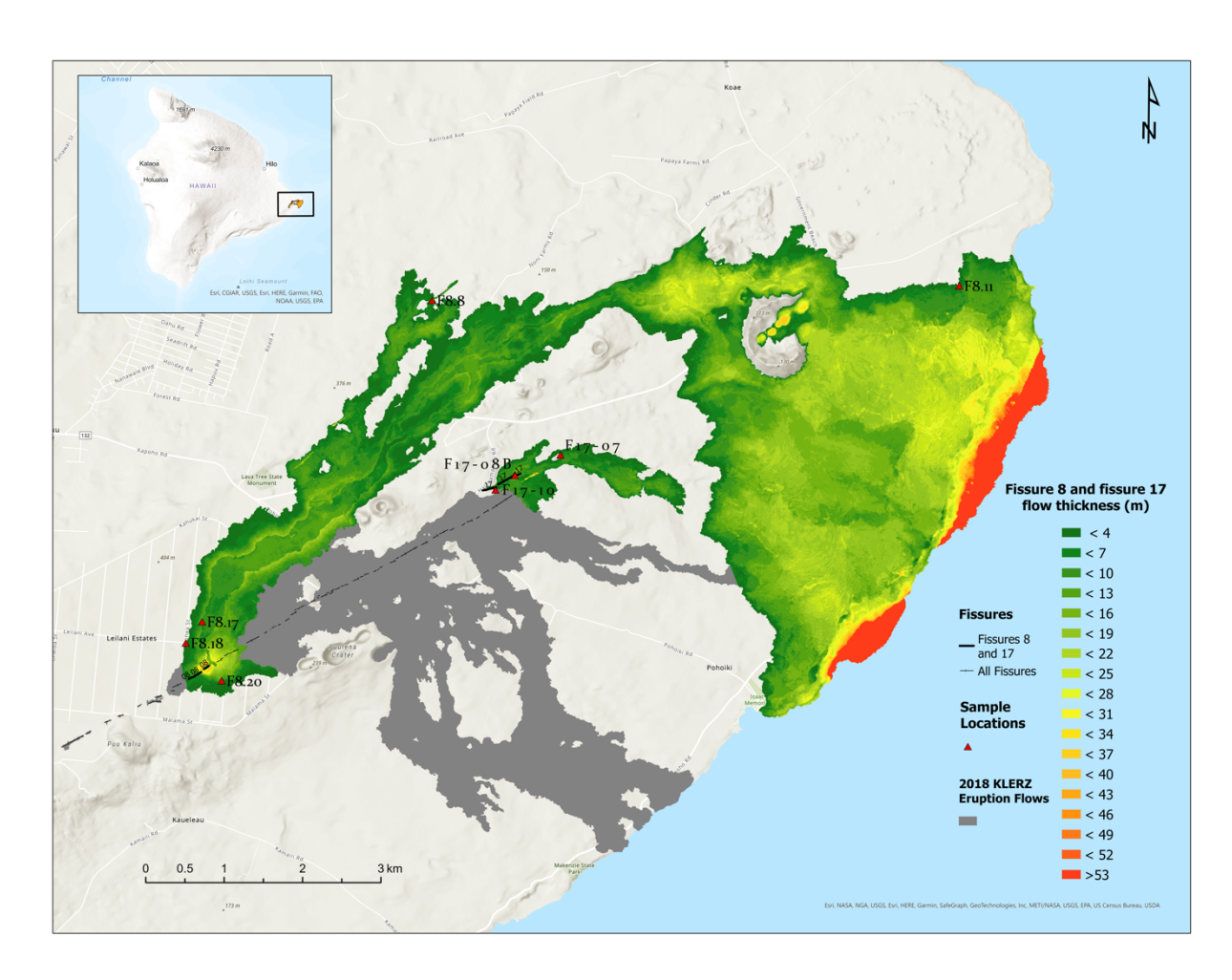
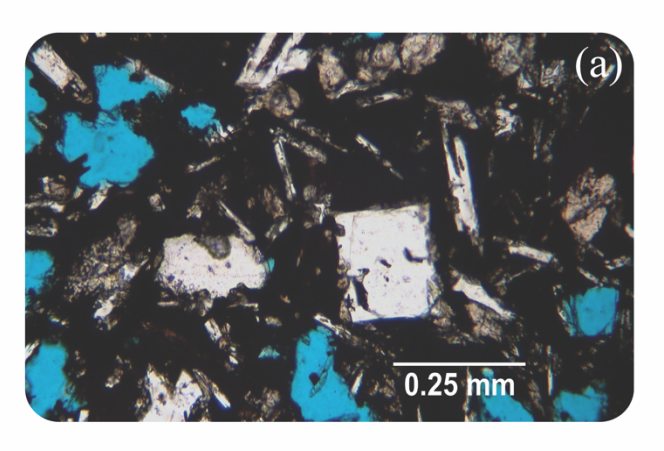
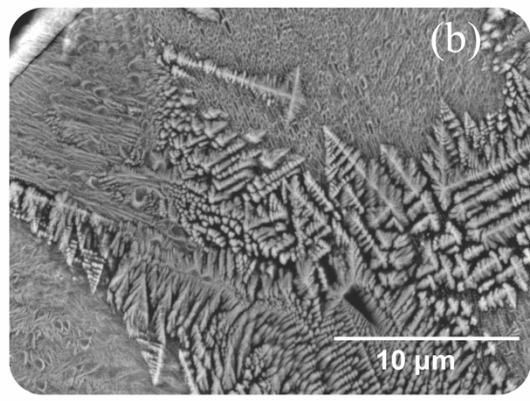


Figure 2: (a) A plane-polarized light image of a sample (F17-07) from the fissure 17 lava flow of the Kīlauea eruption of 2018, where microcrystallinity and intergrowth cause areas to be seen as opaque black, with no way of distinguishing individual grains or any interstitial glass. The blue areas are vesicles filled with dyed epoxy. (b) a BSE image of a sample taken along the fissure 8 lava flow from the Kīlauea 2018 eruption (F8.11), showing bone-marrow-like fronts of incipient crystal formation, which is indistinguishable from any glass that may be left over.





799

800

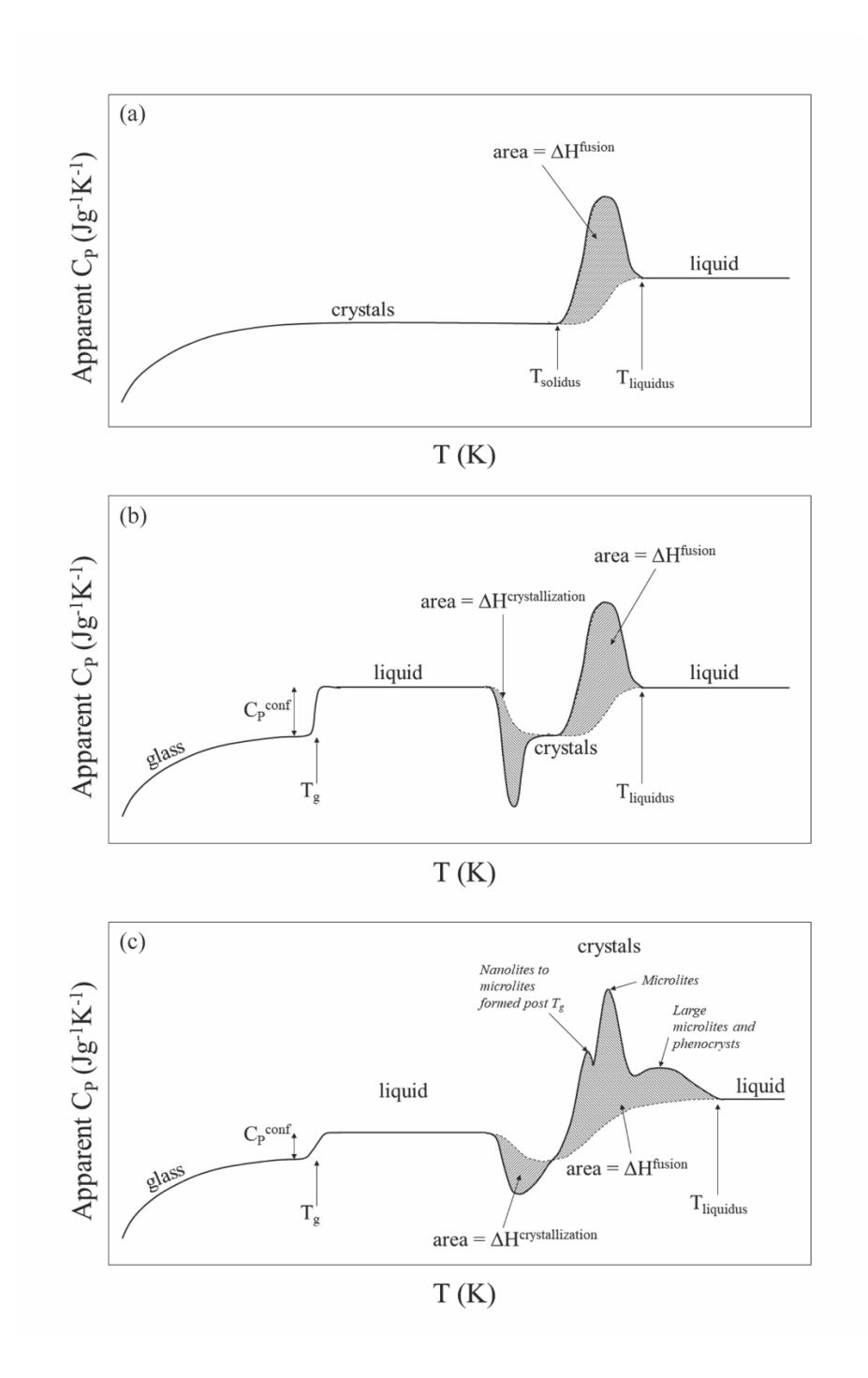


Figure 4: (a) Apparent heat capacity vs. temperature for a sample of lava, initially containing both crystals and glass. (b) Enthalpy vs. temperature diagram for initially glassy and crystalline materials showing the temperature-dependence of the enthalpy of fusion/crystallization. (c) Enthalpy vs. temperature diagram for a sample of lava, initially containing both crystals and glass.

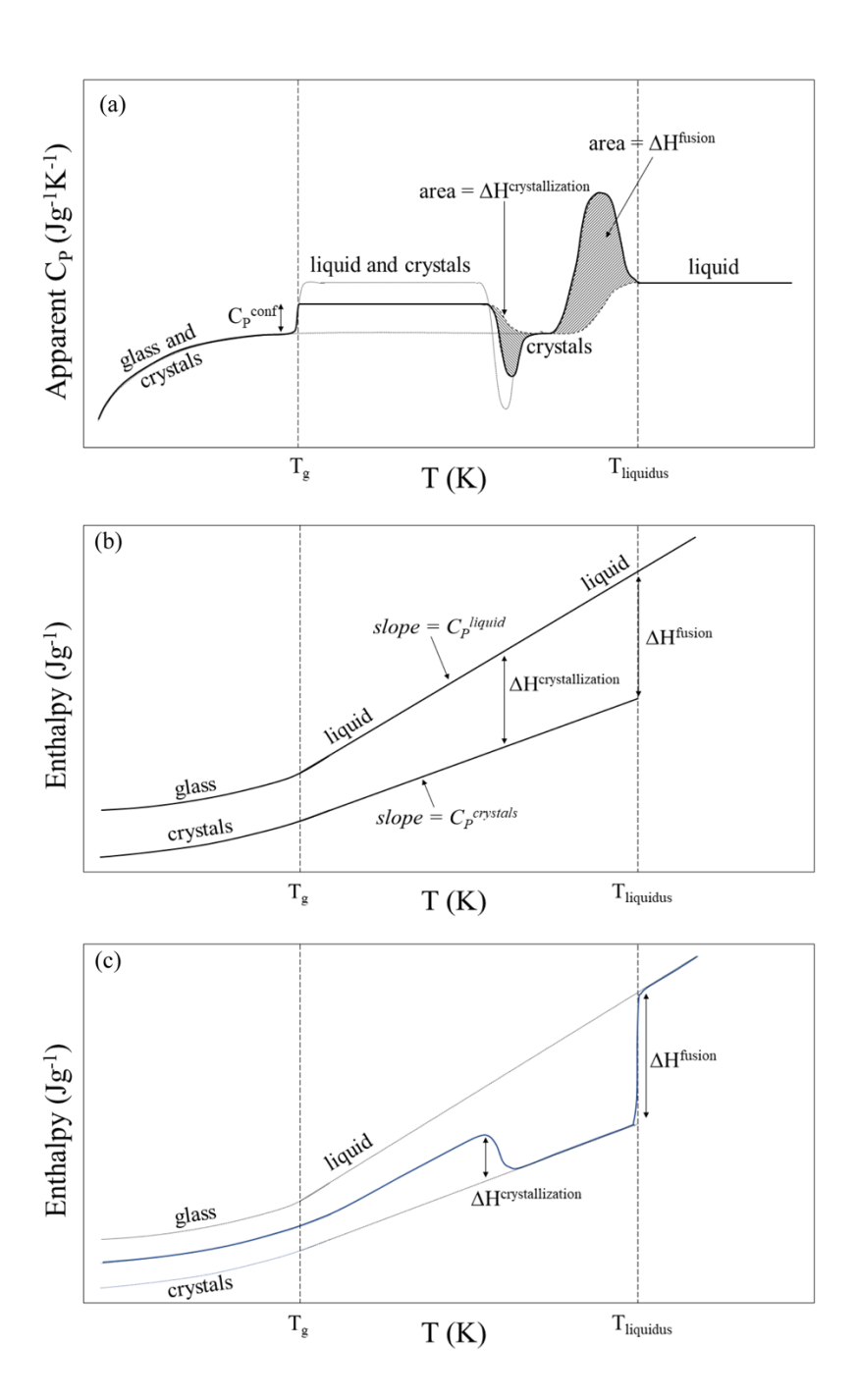
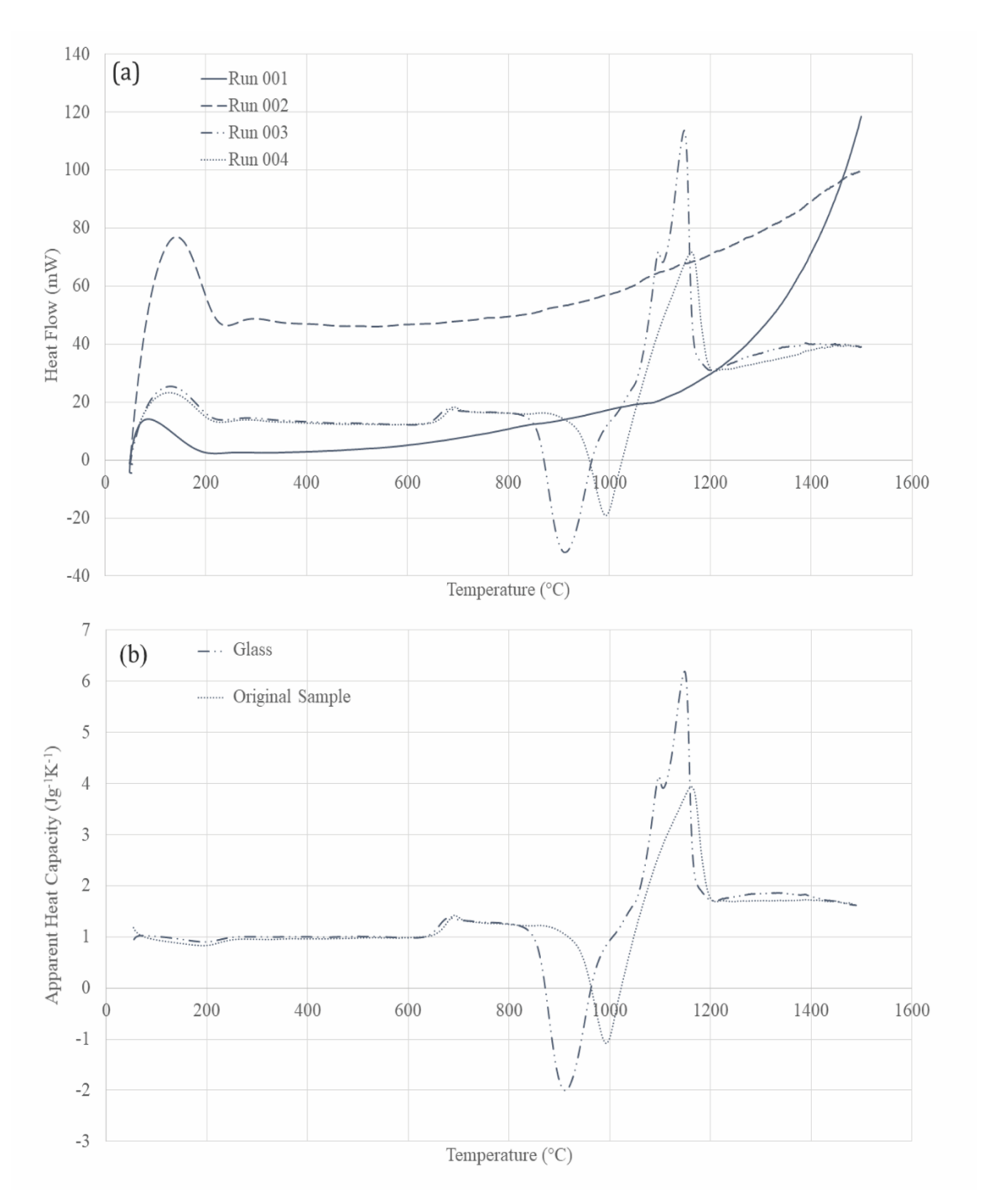
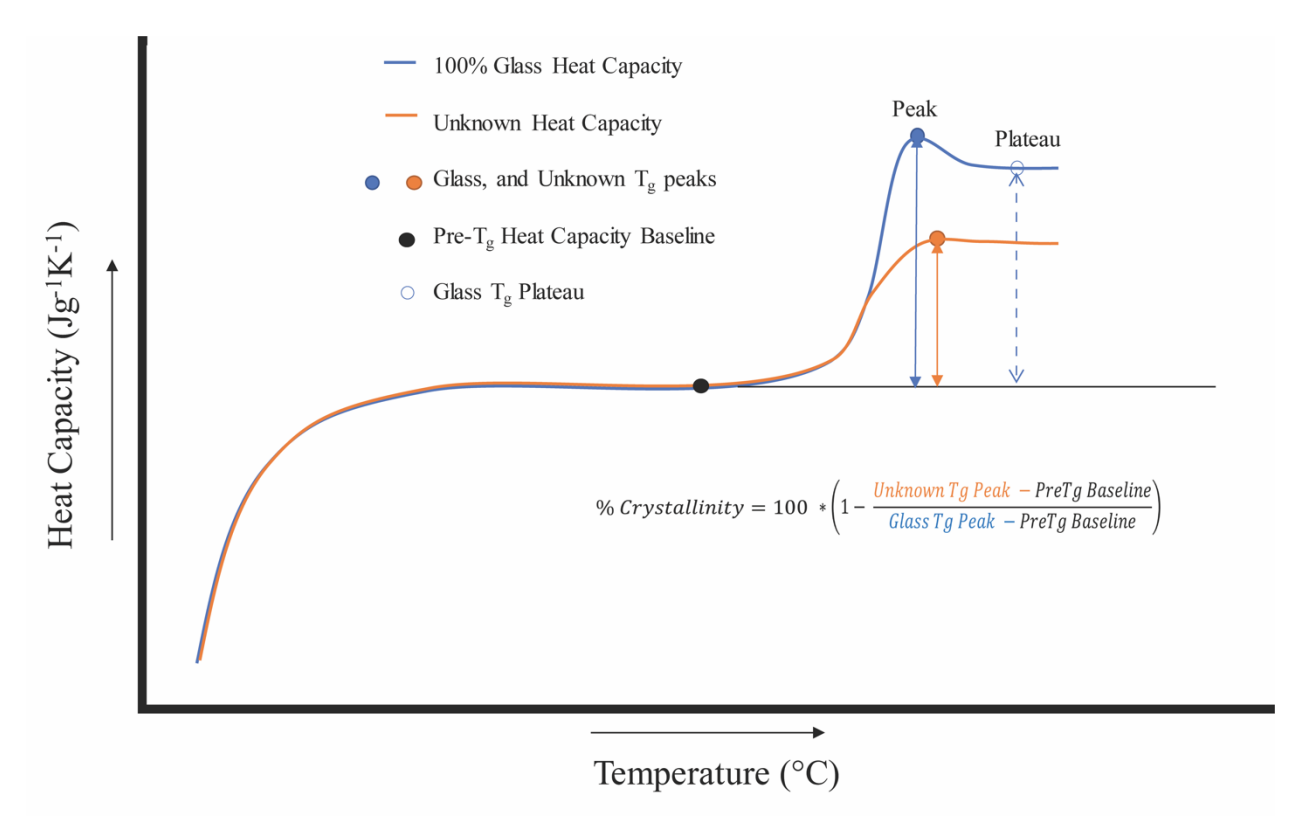
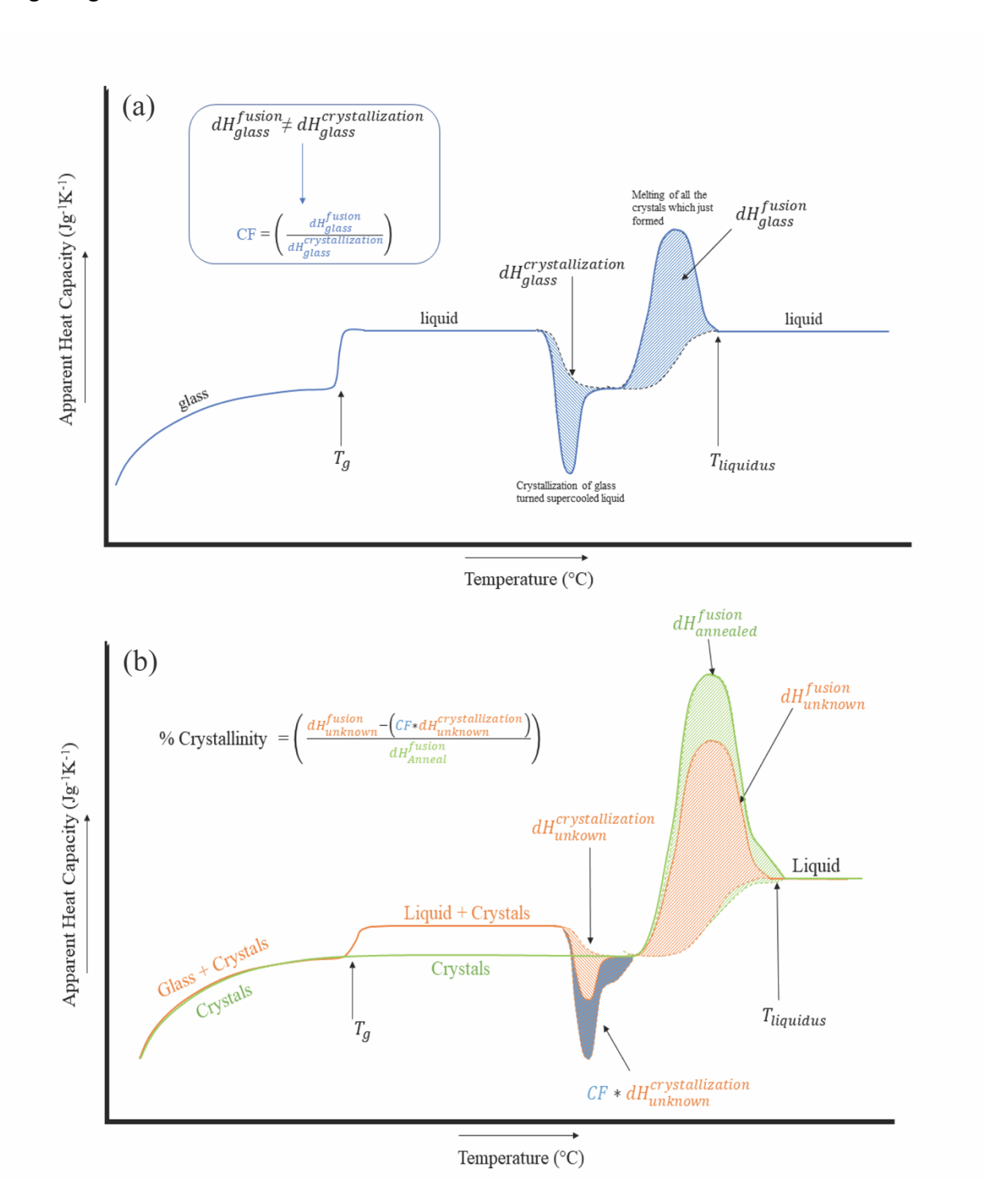


Figure 5: (a) 'Raw' heat flow curves generated by each 'run' done in the differential scanning calorimeter. Run (001) is a blank baseline run where both sample and reference pans remain empty, (002) is a reference run using a sapphire disk in the sample pan, (003) replaces the sapphire disk with the original sample, and (004) is the glass run measuring the quenched material from the (003) run. (b) The two heat capacity curves (original sample and glass) calculated by the four heat flow curves measured by the DSC.







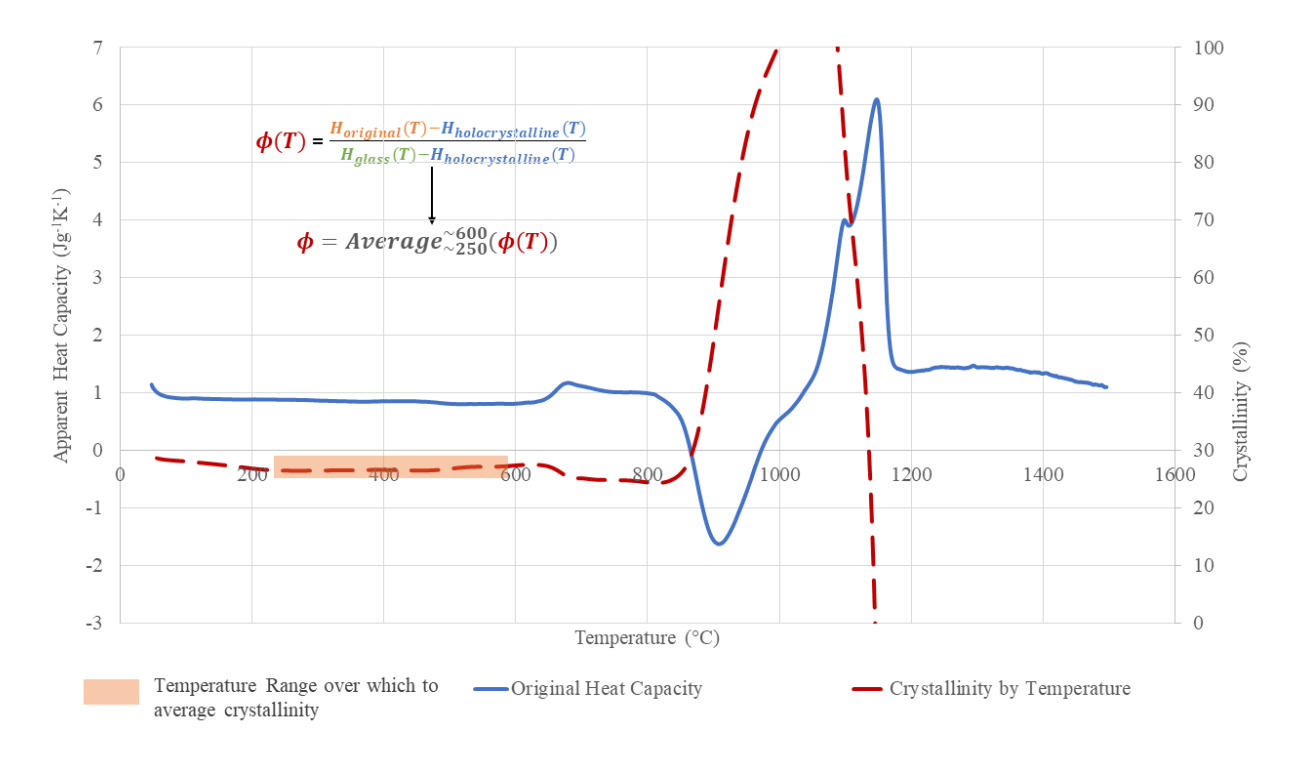


Figure 11: Five fissure 8 lava samples evaluated with standard petrographic techniques for comparison with the DSC methods developed herein. Full-section RGB images (a, d, h, k, and o) are used to determine abundances of the coarsest crystals and provide context for higher-magnification BSE images (b, c, e-g, i-j, l-n, p-q), which capture fine-scale microtexture. Further explanation of the creation of panels a, d, h, k, and o can be found in Figure 12.

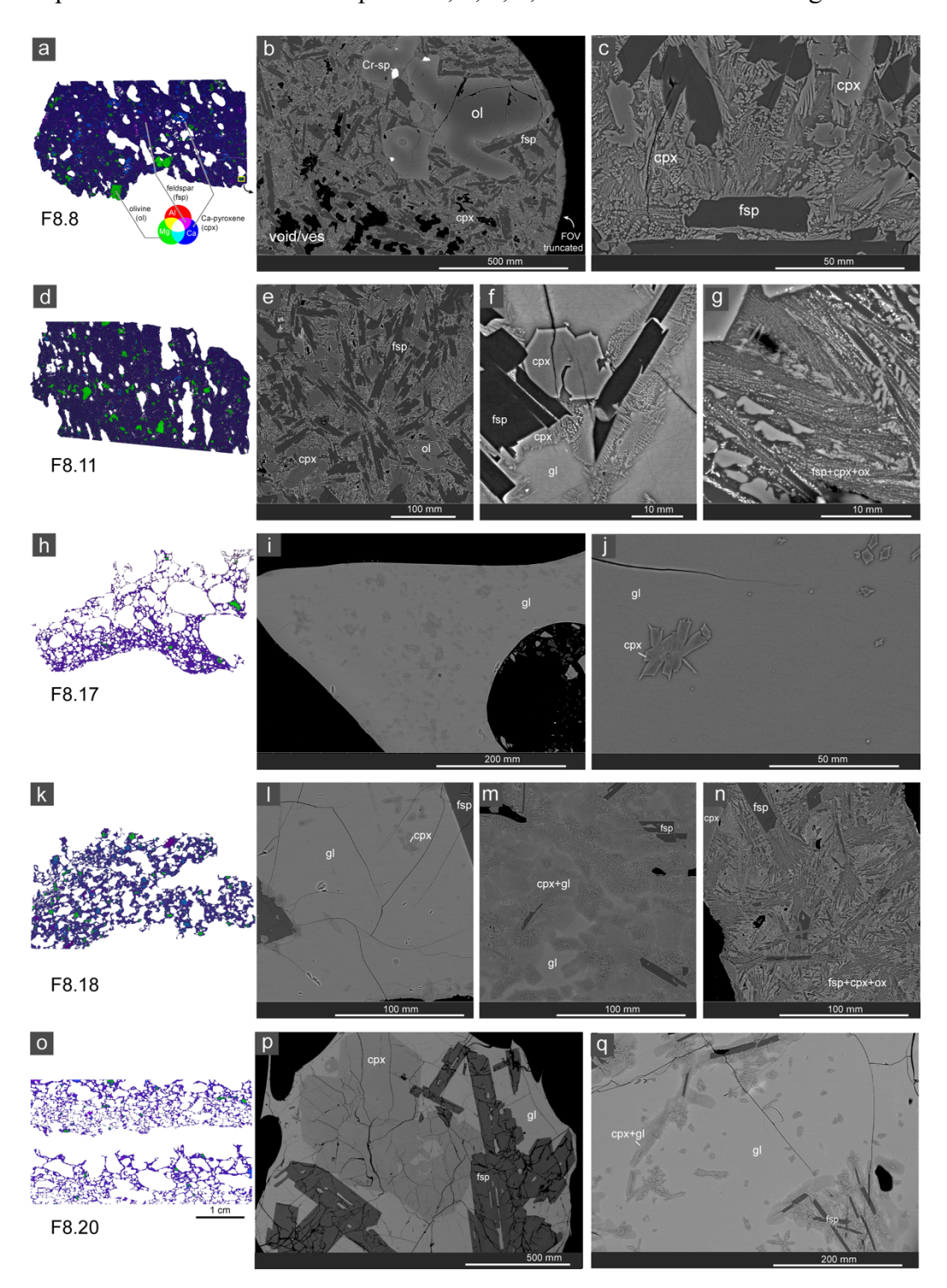


Figure 12: Method of acquiring phase abundances, demonstrated with sample F8.8. Wavelength dispersive spectroscopy (WDS) X-ray intensity maps for elements Al, Mg, and Ca (a-c) are combined as separate channels to create a composite RGB image (d). The epoxy in vesicles and surroundings and the feldspar mounting crystals are manually masked and the sample boundary is identified. Next, phases are segmented manually and filled with designated grayscale values (e). The balance of the sample is allocated "groundmass", which includes undifferentiated glass and fine-grained crystals. Two segmentations provide bracketing estimates of feldspar abundance (f and g). BSE images, collected in a grid pattern from the full section (l), are each approximately the size of the symbol; point counts are conducted on selected images (m). Voids, vesicles, pits, and other imperfections that obscure the phases are excluded (red dots in m) from the point count, as are crystals >150 microns. Higher-magnification BSE imaging is used to define and quantify the abundance of microtexture domains (circular insets), and thus submicron phases. In this case, domain 2 consists of 10 % glass, 68% clinopyroxene microlites, 2% Fe-Ti oxides, and 20% feldspar microlites. Domain 3 has the same phases but in different proportions (5% glass, 45% clinopyroxene microlites, 5% Fe-Ti oxides, and 45 % feldspar). Domain 1, not exhibited in this image or sample, is defined as >95% glass.

847

848

849

850

851 852

853 854

855 856

857

858

859

860

861

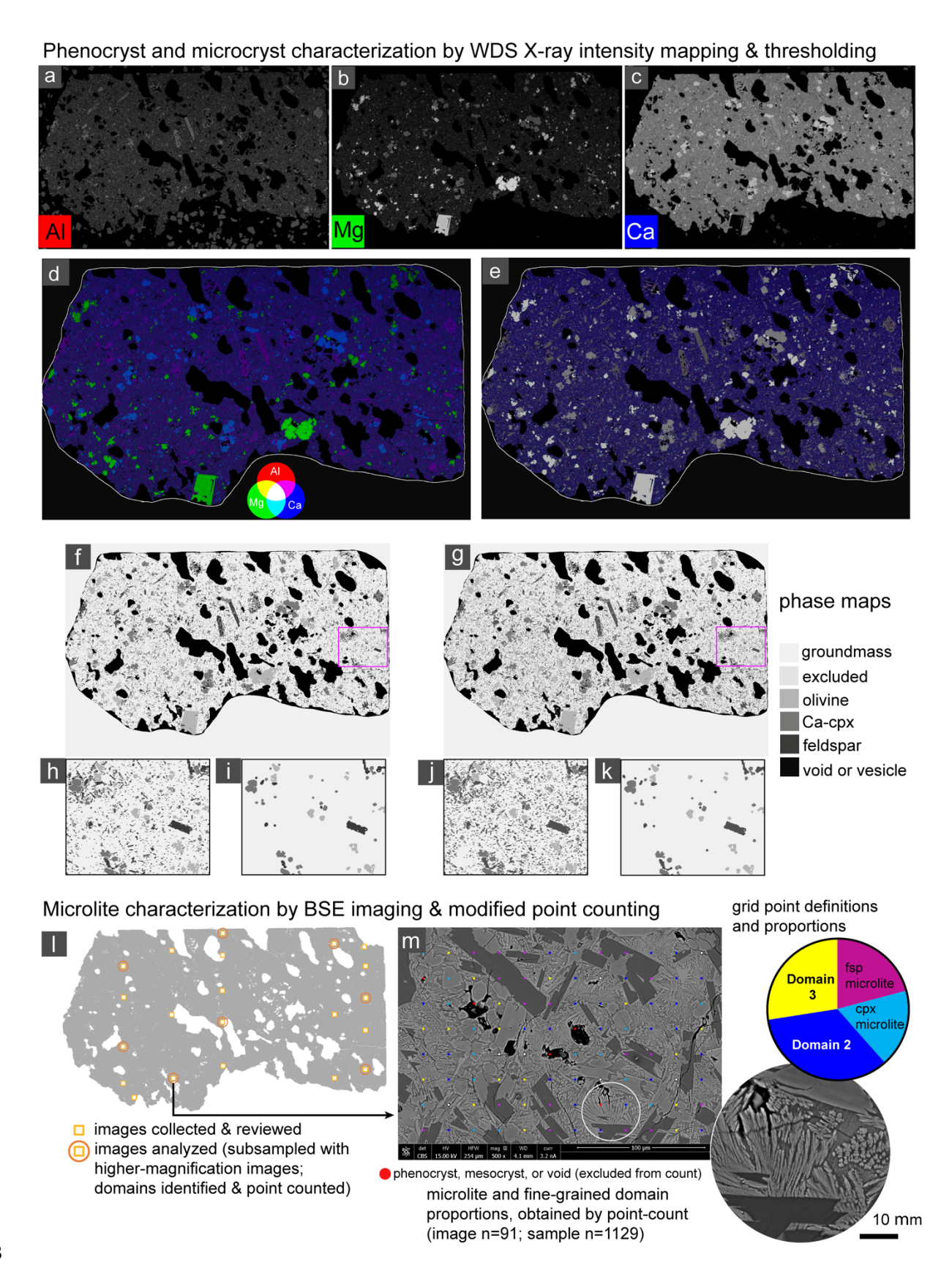


Figure 13: Final calculated configurational heat capacity (CHC) crystallinities in comparison to the BSE/WDS calculated crystallinities. Two possibilities were calculated, using either the peak (light green) or the plateau (dark green) of the glass transition. The values calculated from BSE/WDS methods are shown as the black points. The error bars on the BSE/WDS methods indicate the standard deviation of the analytical method (thick black line) and the 1σ uncertainty due to sample heterogeneity (dotted gray line). The error bars on the calorimetric and enthalpic methods are the maximum 1σ uncertainty calculated.

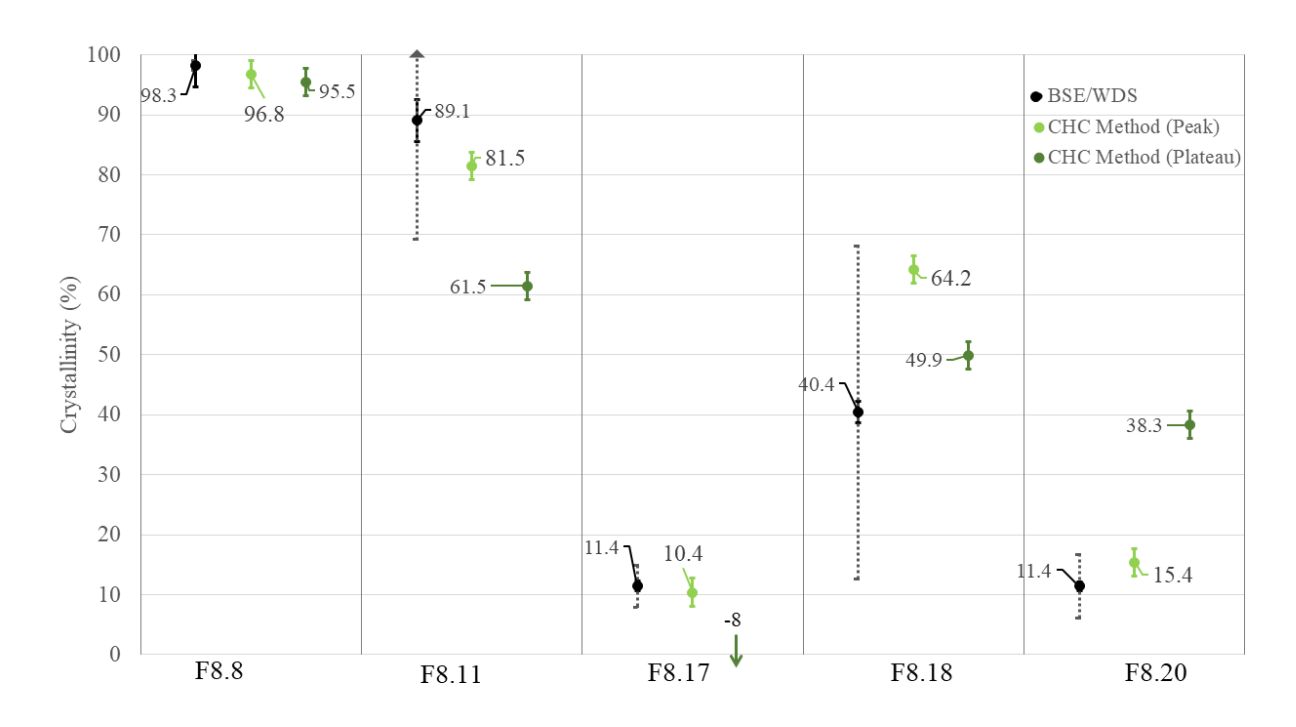


Figure 14: Final calculated enthalpy ratio (ER) crystallinities in comparison to the BSE/WDS calculated crystallinities. The values calculated from BSE/WDS methods are shown as the black points. The error bars on the BSE/WDS methods indicate the standard deviation of the analytical method (thick black line) and the 1σ uncertainty due to sample heterogeneity (dotted gray line). The error bars on the calorimetric and enthalpic methods are the maximum 1σ uncertainty calculated.

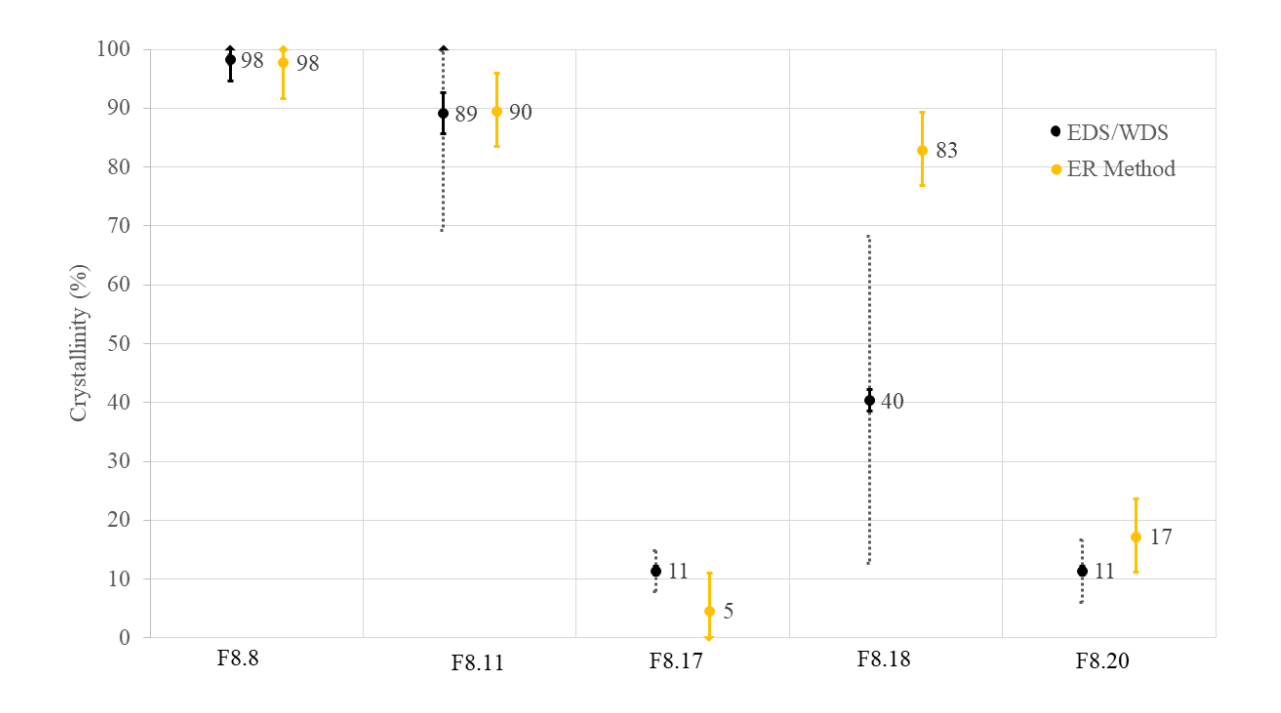


Figure 15: Final calculated Temperature Averaged pre-Tg Enthalpy (TAE) crystallinities in comparison to the BSE/WDS calculated crystallinities. The values calculated from BSE/WDS methods are shown as the black points. The error bars on the BSE/WDS methods indicate the standard deviation of the analytical method (thick black line) and the 1σ uncertainty due to sample heterogeneity (dotted gray line). The error bars on the calorimetric and enthalpic methods are the maximum 1σ uncertainty calculated.



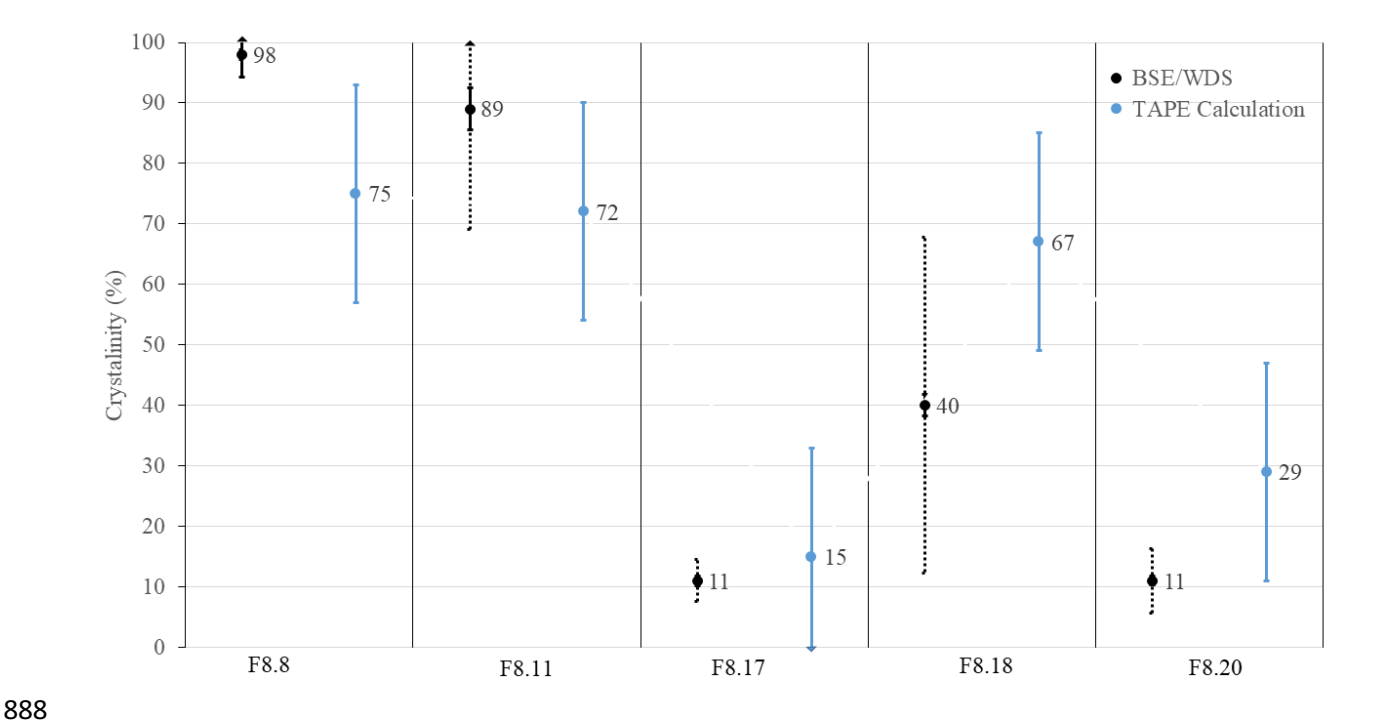


Figure 16: Comparison of the three calorimetric crystallinity methods with the BSE/WDS (black circles) and image thresholding methods (black triangles), for fissure 8 and fissure 17 samples respectively. No CHC plateau calculations were done for fissure 17 samples, due to a lack of any plateau. The error bars on the BSE/WDS methods indicate the standard deviation of the analytical method (thick black line) and the 1σ uncertainty due to sample heterogeneity (dotted gray line). The error bars on the calorimetric and enthalpic methods are the maximum 1σ uncertainty calculated. The error bars on the image thresholding values indicate the range of possible crystallinities between the minimum and 100%, as determined by the ambiguity of the groundmass.



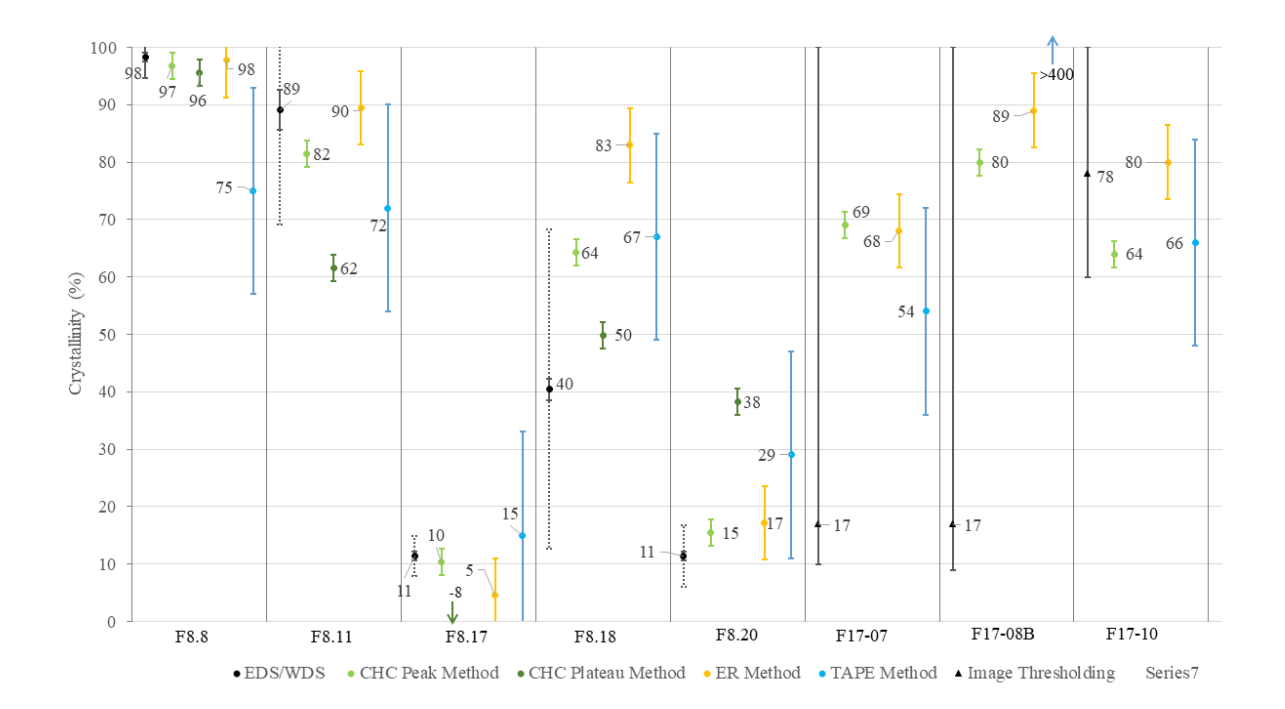


Table 1: BSE/WDS crystallinities by size, with associated total crystallinity uncertainties due to analysis and sample heterogeneity.

	pheno- crysts (v. %)	micro- phenocrysts (v. %)	microlites (v. %)	SUM (v. %)	analytical uncertainty		sample variance ¹	
	120 um - 1000 um	50-120 um	1-50 um	1-1000 um	l stdev	% rel.	1 stdev	% rel.
F8.8	9.5	10	78.8	98	3.7	4%	0.8	1%
F8.11	5.3	6.7	77.1	89	3.5	4%	19.9	22%
F8.17	5.8	1.1	4.5	11	0.8	7%	3.5	31%
F8.18	9.3	6.6	24.5	40	1.8	4%	27.8	69%
F8.20	4	2.1	5.3	11	0.7	6%	5.3	47%

¹ Variance is assessed as a composite of the variance observed at the full-section scale (WDS maps of multiple thin sections) and at the groundmass scale. The variance is chiefly controlled by the variability in the groundmass

Table 2: Fissure 8 sample calculated crystallinities compared to the BSE/WDS crystallinities used for validation.

	EDS/WDS (v. %)	Analytical Standard Deviation (v. %)	Sample Heterogeneity Standard Deviation (v. %)	CHC Peak Method (v. %)	ER Method (v. %)	TAPE Method (v. %)
F8.8	98.3	± 3.7	± 0.8	97 ± 3	98 ± 6	75 ± 18
F8.11	89.1	± 3.5	± 19.9	82 ± 3	90 ± 6	72 ± 18
F8.17	11.4	± 0.8	± 3.5	10 ± 3	5 ± 6	15 ± 18
F8.18	40.4	± 1.8	± 27.8	64 ± 3	83 ± 6	67 ± 18
F8.20	11.4	± 0.7	± 5.3	15 ± 3	17 ± 6	29 ± 18

	Image Thresholding Average	Image Thresholding Minimum-Maximum	CHC Peak Method	ER Method	TAPE Method
F17-07	17	10-100	69 ± 3	68±6	54 ± 18
F17-08B	17	9-100	80 ± 3	89 ± 6	>400 ± 18
F17-10	78	60-100	64±3	80 ± 6	66 ± 18

912